TECHNISCHE UNIVERSITÄT WIEN

DIPLOMARBEIT

Simulation of X-ray photoelectron spectra beyond the quasi-elastic approximation: application to nanoparticle analysis

zur Erlangung des akademischen Grades

Diplom-Ingenieur

im Rahmen des Studiums

Technische Physik

eingereicht von

Martin Hronek
Matrikelnummer 00525260

ausgeführt am Institut für Angewandte Physik
der Fakultät für Physik der Technischen Universität Wien

Betreuung durch
Betreuer: Ao.Univ.Prof. Dr.techn. Wolfgang Werner

Wien, 03.05.2019

(Unterschrift Verfasser/in) (Unterschrift Betreuer/in)

Abstract

The subject of this thesis is the quantification of shell thicknesses of core-shell nanoparticles (CSNP) by means of electron beam techniques, in particular X-ray photoelectron spectroscopy (XPS).

For that purpose round robin XPS experiments with associated institutes were performed. The resulting XPS peak intensities were evaluated and compared, with a very good agreement over all involved laboratories. To get a better understanding of the investigated CSNP additional and complementary transmission electron microscopy (TEM) experiments were performed. A comparison of the experimental results shows a variety of asymmetries in the investigated sample which have a noticeable impact on simulated spectra with ideal geometry CSNP.

SESSA (Simulation of Electron Spectra for Surface Analysis), a database developed with the National Institute of Standards and Technology (NIST) utilizes the efficient quasi-elastic approximation (QEA) for the spectra calculations. However this approximation disregards the energy dependency of the elastic and inelastic scattering events which is only valid in a small energy domain.

A physically more realistic Monte Carlo simulation method was tested and implemented into SESSA. With the help of this newly implemented *true slowing-down* (SDN) method the currently used QEA could be refined and a physical more realistic approximation could be implemented. These more realistic approximations (QEA+ and QEA*) were compared to the present methods and successfully tested.

This effort was made to simulate the background of an X-ray photoelectric spectrum more precisely and therefore be able to use it as an additional analytical tool for dimensional measurements of core-shell nanoparticles and other complex sample morphologies.

Finally, as part of the 14IND12 Innanopart project funded by the European Metrology Programme for Innovation and Research (EMPIR) simulations of acentric cores and pores in powders and single sphere geometries were performed, which model the observed features to estimate the impact on the shell thickness determination.

Kurzfassung

Das Thema dieser Arbeit umfasst die Quantifizierung von Schalendicken von Kern-Schale-Nanopartikeln (core-shell nanoparticles, CSNP) unter der Verwendung von Elektronenstrahltechniken, im speziellen der Röntgenphotoelektronenspektroskopie (X-ray photoelectron spectroscopy, XPS).

Für diesen Zweck wurden XPS-Experimente in einem Ringversuch mit Partnerinstituten durchgeführt. Die Ergebnisse und die daraus resultierenden Peakintensitäten wurden ausgewertet, sowie verglichen. Diese Resultate zeigten sehr gute Übereinstimmung über alle beteiligten Laboratorien. Um ein tieferes Verständnis über die untersuchten CSNP zu erhalten, wurden zusätzlich ergänzende Experimente mit Hilfe der Transmissionselektronenmikroskopie (TEM) durchgeführt. Der Vergleich der experimentellen Ergebnisse zeigte eine Reihe von Asymmetrien in den zu untersuchenden Proben. Diese Besonderheiten haben merkbare Auswirkung auf simulierte XPS-Spektren, verglichen mit Spektren von idealen Kern-Schale-Nanopartikeln.

SESSA (Simulation of Electron Spectra for Surface Analysis), eine Datenbank entwickelt mit dem National Institute of Standards and Technology (NIST) verwendet die quasi-elastische Näherung (quasi-elastic approximation, QEA) für die XPS-Spektrenberechnung. Jedoch vernachlässigt diese Näherung die Energieabhängigkeit der elastischen und inelastischen Stoßvorgänge von Elektronen, was nur in einem sehr kleinen Energiebereich gültig ist.

Zusätzlich wurde als Teil dieser Arbeit eine physikalisch realistischere Monte-Carlo Simulationsmethode getestet und in SESSA implementiert. Mit dieser neu implementierten *true slowing-down* (SDN) Methode wurde die aktuell verwendete QEA-Methode verfeinert und erweitert. Diese physikalisch realistischere Näherungen (QEA+ und QEA*) wurden mit der bestehenden Methode verglichen.

Diese Bemühungen wurden getätigt, um den Signaluntergrund von Röntgenphotoelektronenspektren präziser zu simulieren und infolgedessen jenes Untergrundsignal als weiteres analytisches Werkzeug zur Dimensionsbestimmung von Kern-Schale-Nanopartikeln und weiteren komplexen Probenmorphologien zu verwenden.

Darüber hinaus wurden als Teil des 14IND12 Innanopart Projektes, welches vom europäischem Metrologieprogramm für Innovation und Forschung (European Metrology Programme for Innovation and Research - EMPIR) finanziert wird, XPS Simulationen von Einzelkugel- und Pulvergeometrien mit a-zentrischen Kernen und Poren durchgeführt,

welche die gefundenen Besonderheiten nachbilden um deren Einfluss auf die Schalendickenbestimmung abzuschätzen.

Contents

1 Introduction

Nanotechnology is used in an increasing number of products all around us, starting from technological products such as photovoltaic cells and surface treatments (e.g. coatings), medical applications (e.g. drugs and contrast agents [1]) and personal care (e.g. deodorants and sun creams), as well as consumer products in cosmetics (e.g. lip gloss) and foods (e.g. peanut butter and other sweets). Due to this wide adoption it's important to be able to measure and assess the used materials and the quality of these products.

Nanotechnology is internationally defined by the *ISO/TS 80004-1:2015* norm from the International Organization for Standardization.[2] This technology commonly utilizes nanomaterials which are materials on a nanoscopic scale.[3] The term nanoscopic scale states that one or more spatial dimensions is in the size range of $1 - 100nm$. In 2011 the European Union has adopted the definition brought up by the commissions recommendation on the definition of nanomaterial *EU 2011/696*.[4] This recommendation was just one step of many, starting from 2009 by an resolution in the European Parliament followed by the reference report *Considerations on a Definition of Nanomaterial for Regulatory Purposes* from 2010 created by the European Commissions Joint Research Centre.[5]

All this effort has been done for the intrinsic property of nanomaterials being in the nanoscopic scale. In these dimensions the materials chemical and biological characteristics and properties change due to the rising impact surface area effects have. These changes could also impact the toxicity a material has for the human body.[6, 7, 8] Although this might have negative effects, based on the same property, nanomaterials could also have very positive effects in the same area of medicine on the human body. Such as controlled and targeted drug delivery minimizing side-effects and increasing drug efficiency (e.g. in cancer therapy). [9, 10, 11]

As already stated nanomaterials are getting more abundant in our environment. Due to the possible nanotoxicity, regulations will become more frequent taking into account the dimension of materials as already seen in the regulations *EC 1223/2009* and *EU 1169/2011*. In which the European Union created obligatory labelling regulations for cosmetics and food products containing engineered nanomaterials. Engineered nanomaterials was later defined in regulation *EU 2015/2283* which focuses on novel foods.[12, 13, 14]

As a consequence this will create additional demand for the industry and regulators to determine such nano dimensions, sizes and further specific details about the used nanomaterials. Innanopart is a project funded by the European Metrology Programme for

Innovation and Research (EMPIR) participating states and the European Unions Horizon 2020 program, with the goal to develop and establish methods of quantification and standardise methods for measuring chemical compositions and thickness of nanoparticle shells. [15]

Core-shell nanoparticles (CSNP) in particular are very interesting for medical and technological applications due to their geometry, dimensions and the resulting unique surface-volume ratio. Ideal CSNP have a spheric core with a concentric shell around it. Sphere and core usually consist of different materials creating a particle with special properties. These specially constructed particles are also often referred to as functionalized particles, because their shell and consequently their new surface changes the particles physical and chemical properties.

Different methods of measuring these CSNPs exist and could be used in determining the diameter and the core-shell dimensions. One can get transmission electron microscopy (TEM) pictures of a certain CSNP and compare it to a geometric model. Transmission electron energy loss spectroscopy (TEELS) gives information about the chemical composition and mapping of the particles. Another method used for identifying the chemical composition and getting an estimation of the geometrical distribution is the energy dispersive X-ray spectroscopy (EDX) in TEM. While in TEM images, single visualizations of particles can be obtained which then are visually analysed. The XPS method usually produces a sum over area spectra, hence giving an average and therefore typical size of the investigated particles. Another big benefit of XPS is that the amount of material is directly measured and therefore the signal already delivers precise quantifiable values. Furthermore in the XPS data the chemical composition of materials could be found and so the different bonding states are available for further analysis.

An approach used to extract information out of XPS spectra is by comparing the shell peak intensity signal to the core peak intensity signal. Although there are other methods (T_{NP} Formula [16], IC model [17]) which can be used to calculate the dimensions of such particles with similar or better accuracy, all of them neglect the majority of the collected electrons since the background shapes are not taken into account.

In general the background of an XPS spectrum is the collection of all electrons which have lost energy due to at least one inelastic collision. As shown by S. Tougaard [18] the background shape of an XPS spectrum could be used to obtain more information about the sample and therefore constitutes an additional analytical tool.

In this present work, model core-shell nanoparticles with a Poly-Methyl-Methacrylate (PMMA) shell and a Poly-Tetrafluor-Ethylen (PTFE) core where investigated by means of different methods. Simulations of CSNPs were created to understand different effects geometrical abnormalities could have on XPS spectra. Additionally a complex Monte Carlo model for XPS spectrum simulations was implemented which resulted in an improvement of an efficient algorithm currently in use.

2 Methodology

This chapter gives a short introduction on the physical and technical fundamentals that later data and arguments will be based on. For a more detailed review the reader is referred to [19], [20] and [21].

2.1 X-ray photoelectron spectroscopy

X-ray photoelectron spectroscopy (XPS) was developed in the late 1950s by Siegbahn and colleagues. In early times it was also referred to as electron spectroscopy for chemical analysis (ESCA) since the technique has the ability to gather information about the chemical state of an investigated sample and not only the elemental composition of it. [1]

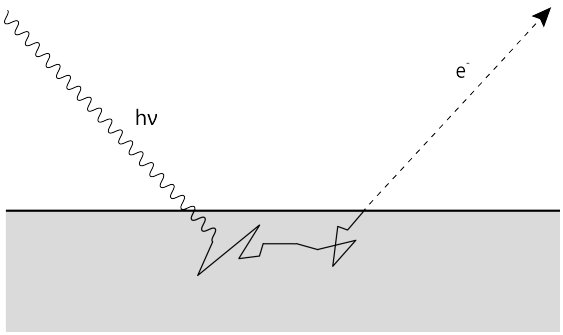

Figure 2.1: Schematic processes in X-ray photoelectron spectroscopy, Photons interacting with the sample generating photoelectrons which lose energy due to occurring incidence inside the material.

XPS is a technique where X-ray photons irradiate a sample and due to photon-matter interaction photoelectrons are freed from their bound states. Those photoelectrons travel inside the sample and interact with the ionic and electronic subsystem of the material via the Coulomb force. Eventually some photoelectrons leave the sample, are detected and form a spectrum. A schematic representation is visualized in Figure 2.1.

Typical energies of X-rays (Figure 2.4) used for XPS are in the range between a few

[1] Siegbahn ended up receiving a Nobel Price in 1981 for his contribution to the development of high-resolution electron spectroscopy.[22]

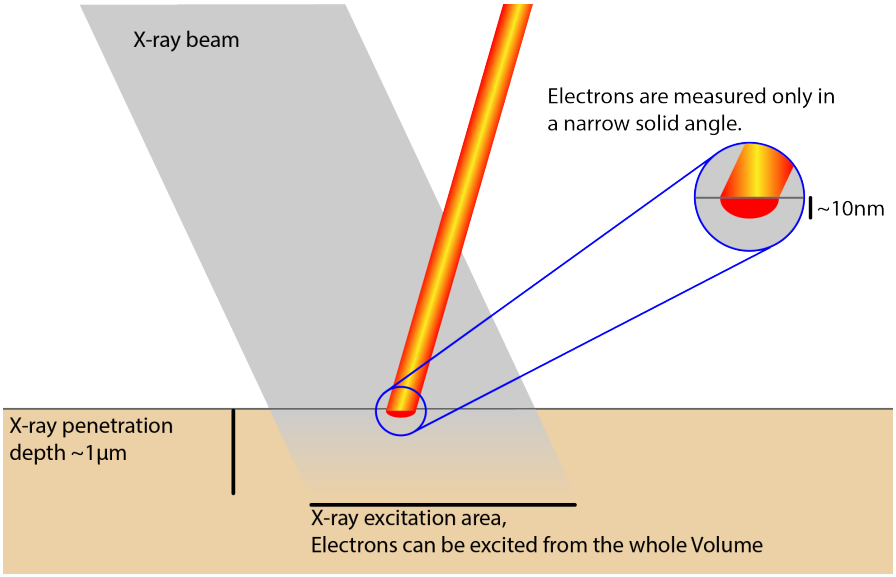

Figure 2.2: Information and penetration depth of X-ray photons and photoelectrons.

hundred eV up to $10s$ of keV. In this energy range, photons interact with matter mainly via the photoelectric effect (Figure 2.5).[23]

Due to the weak interaction with matter the utilized photons penetrate the sample in the μm range. This attenuation is given by a Beer-Lambert type law:

$$I = I_0 \cdot exp(-Ad). \tag{2.1}$$

Were the intensity I is the result of the initial intensity I_0 exponentially decreased by the depth or thickness d and an absorbtion coefficient A.

In contrast to the created photoelectrons which have an average mean free path in the nm range the X-ray photons produce photoelectrons much deeper inside the material than from which these photoelectrons could escape. (Figure 2.2)

The photoelectric (PE) effect may be viewed as transforming the energy from the X-ray photon into the kinetic energy of an excited electron. The occurrence of this interaction is given by the photoelectric interaction cross section were a crude approximation is written as: [24]

$$\sigma = constant \cdot \frac{Z^n}{E^m} \propto \left(\frac{E_b}{h\nu}\right)^{7/2}. \tag{2.2}$$

Here Z is the atomic number with n being range of 4 and 5, E is the photon energy with m ranging from 1 to 3. Further detailed description can be found in the subsection 2.1.1.

A very important distinction of XPS which was additionally promoted and emphasized by using the abbreviation ESCA (electron spectroscopy for chemical analysis) by Sieg-

bahns research group, is the fact that one gets additional information about the chemical environment the photoelectron is ionized from. This is based on the different chemical bonds an atom forms when building up a solid. Due to these bonds the inner electrons are bound tighter to the atom core and thus are slightly shifted in energy. This energy shift can be measured and is characteristic to a chemical bond. (Figure 2.3)

As already can be understood X-ray photoelectron spectroscopy uses X-ray photons to ionize electrons inside an investigated sample. These so called photoelectrons hold some amount of characteristic kinetic energy according to the element and chemical environment they where freed from. Consequently this would already produce a spectrum with different peaks and peak intensities according to the amount of material there is in the investigated sample. However the freed electrons are within the sample and first have to travel from inside the material out. Here the photoelectrons could undergo further electron-matter interactions. These interactions result in further attenuation of the electrons, similar to the photon attenuation this is written as equation (6.3) in [19]:

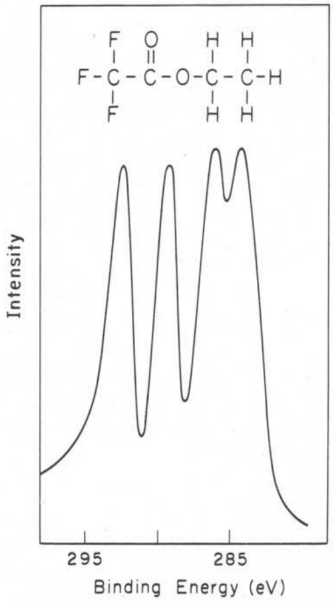

Figure 2.3: XPS spectrum for C1s peak with Carbon atom contributions of an molecule from an investigated sample.[25]

$$I = I_0 \cdot exp(-\frac{s}{\lambda}) \tag{2.3}$$

Were the resulting intensity I is an exponentially decayed initial intensity I_0, with s being the travelled path length and λ the mean free path the electron can travel on average without any interaction. According to the charge an electron has, it is influenced by the electromagnetic force and thus any atom or charged particle. This is also the reason for their short mean free paths electrons can travel without interruption in comparison to photons. Explaining the nature of why XPS is such a surface sensitive measurement method.

More in depth information about the different electron-matter interactions can be found in subsection 2.1.2.

The nature of electrons adds further experimental difficulties. Because of their short mean free paths this measurement method is usually done under ultra high vacuum with values of below 10^{-7} millibar.

More details about experimental conditions can be found in subsection 2.1.4.

2.1.1 Photon-Matter interaction

The underlying principle of X-ray photoelectron spectroscopy draws from the fundamental interaction between photons and matter. According to the energy of the incoming electromagnetic waves different phenomena occur in a solid.[23] Since XPS utilizes soft X-rays (Figure 2.4) with energies around 1-10keV we are mainly interested in the low energy phenomena of the photoelectric effect (Figure 2.5). Historically also referred to as the Hallwachs effect. This effect was investigated and described by many scientists such as Hertz, Hallwachs, Stoletov, Lenard, Einstein and Millikan to name a few.

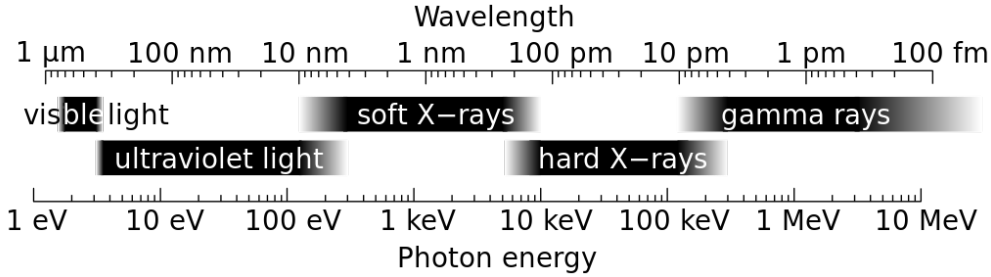

Figure 2.4: Relevant X-ray regions of wavelength (top) and photon energy (bottom), taken from [26]

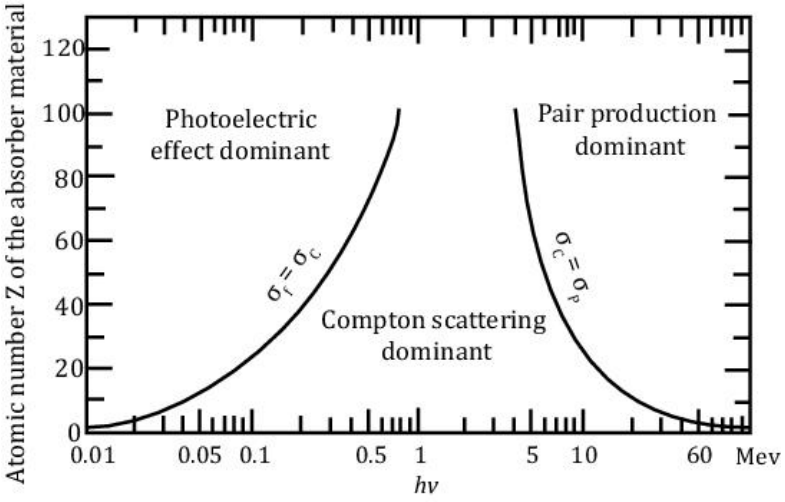

Figure 2.5: Relative importance of Photoelectric effect, Compton scattering and Pair production as a function of photon energy (ordinate scale) and atomic number (coordinate scale), figure 26 from [27] based on figure 1.1 of [23] page 712

In essence the photoelectric effect describes the process in which the energy from an incoming photon excites an electron which is freed from the illuminated material. For

an excited electron to actually escape from a sample, it has to overcome the materials binding effects. One can think of these binding effects as an energy well E_B^v to overcome, which is the difference between the vacuum level and the highest occupied electron state. The incoming electromagnetic (EM) wave has an energy of $E_{photon} = h\nu$, where h is the Plancks constant and $\nu = f$ is the frequency of the wave.[2]

$$E_{kin_{max}} = h\nu - E_B^v \tag{2.4}$$

This energy well or virtual binding energy E_B^v could be composed out of different parts. In metals for example, one specifies the Fermi level as the energy zero reference and the difference to the vacuum level as the material specific work function Φ. With the energy reference defined, one can specify the energy state the electron is excited from. For an electron excited from the state k one can write $E_B^F(k)$. For conducting samples in XPS (Figure 2.6) the vacuum level changes since the Fermi levels can equilibrate and the work function of the sample is replaced by the spectrometer work function Φ_{spec}.

For insulators and semiconductors the energy reference is not clearly defined, due to a more complex band structure with a possible energy gap between the valence and the conduction band. Further difficulty in finding a properly defined energy reference is the electrical non conductivity of semiconductors and insulators which might lead to charging effects, adding complexity to the energy measurement. Those charging effects can distort the measured spectra in different ways. Details about charging effects and charge compensation in XPS can be found in chapter 8 of [20] and chapter 6.3 of [29].

Since EM-waves excite quantized bound electrons the wave-particle duality has to be taken into account. With the help of quantum theory and the Schrödinger equation one can describe the interaction of the bound electron with an EM-wave by using the perturbation theory and Fermis golden rule. The time-independent Schrödinger equation describes the unperturbed atom via its systems Hamiltonian $\hat{H}_0$ and the bound electrons wave function $|\Psi_n\rangle$ with its energy Eigenvalue E_n (See chapter 9.2 of [19] for further details.):

$$\hat{H}_0 |\Psi_n\rangle = E_n |\Psi_n\rangle \tag{2.5}$$

The rate of transition between the initial $|\Psi_i\rangle$ and final $|\Psi_f\rangle$ state is calculated by:

$$\lambda_{i\to f} = \frac{2\pi}{\hbar}\rho(E_f)\left|\langle\Psi_f|\,\hat{H}'\,|\Psi_i\rangle\right|^2. \tag{2.6}$$

It takes into account the perturbed Hamiltonian $\hat{H}'$ and the density of final states $\rho(E_f)$. A detailed derivation of Fermis second golden rule can be found in [30] and chapter 9.10.1

[2] This is based on Albert Einsteins work [28].

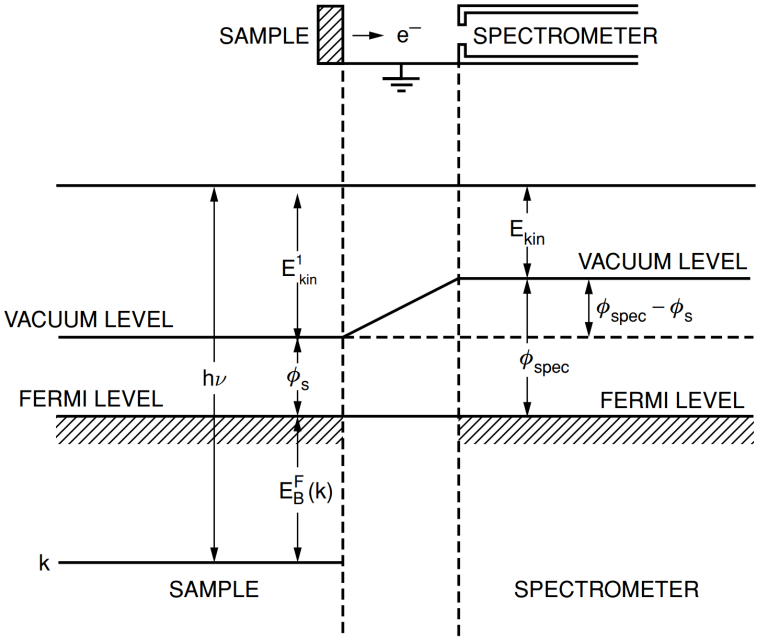

Figure 2.6: Schematic of relevant XPS energy levels for conductors, from [19] Fig. 10.6

of [19]. [3]

To fully describe the interaction process the photon ionization cross section is calculated as:

$$\sigma = \frac{\lambda_{i \to f}}{J}. \tag{2.7}$$

Taking into account $\lambda_{i \to f}$ the transition probability over time and J the EM flux, as the number of particles over area over time. Details can be found in chapter 9.6 of [19].

Modern calculations of these photoelectron ionization cross sections can be found in [33] and [34].

2.1.2 Electron-Matter interaction

An introduction of the overall process for X-ray photoelectron spectroscopy was discussed in section 2.1. X-ray photons are illuminating a sample from which electrons are release with characteristic energies.

In the sample the probing entity changes from the uncharged photon to a charged electron particle, due to the photoelectric effect as described in subsection 2.1.1. Following the excitation of a photoelectron consequent effects as the Auger-Meitner effect[4] or X-ray

[3] Based on Diracs formula (32) in [31] and Fermis formula VIII.2 in [32]
[4] Meitner described the same effect before Auger in 1922.[35]

fluorescence could occur. Since the previously excited photoelectron is leaving an empty state E_l behind a probability exists for a bound electron E_h, from a higher state, to refill this open state. The energy difference $E_h - E_l$ could allow another loosely bound electron near the Fermi edge to escape the binding effects of the atom and therefore create a second unbound electron, also referred to as an Auger electron. The yields for the Auger process and the X-ray fluorescence process are complementary. For atomic numbers around $Z >\sim 30$ the fluorescence process is about equally probable as the Auger process and with rising atomic numbers X-ray fluorescence becomes more likely to occur. (Figure 2.7)

More on this topic can be found in chapter 12.3 of [19].

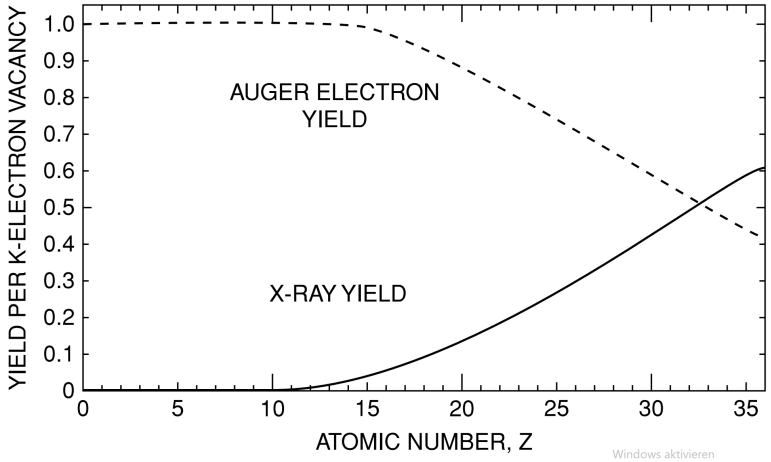

Figure 2.7: Process yield per vacant electron for different atomic numbers, taken from [19] Fig. 12.5.

These unbound photo- and auger electrons now become the main point of interest since they convey information about the sample. The electrons behaviour inside the specimen is different from photons as they are charged particles and thus interact differently with the electromagnetic fields of the atoms and electrons within the solid.

The electron interaction processes within the specimen can be differentiated as elastic and inelastic scattering. The elastic processes feature the property of preserving the kinetic energy of the incident electron although the direction is not conserved and large momentum changes are undergone. In contrast electrons in an inelastic scattering process transfer parts of the projectiles kinetic energy to their scattering partner. Therefore these inelastic processes do not conserve the projectiles kinetic energy.

These differences are understood as the scattering targets masses differ for the inelastic and elastic processes. The Born-Oppenheimer approximation is a good example for the validity of this differentiation, here the heavy and thus slowly moving nuclei lattice is separated from the lighter electrons.

Due to the differences in properties of photons and electrons and consequently their interaction with matter, X-ray photons can penetrate into the sample according to their energy in a μm range whereas the electron interaction processes in this energy range have a mean free paths in the nm range. Therefore an excited electron might scatter multiple times until it leaves the sample. Furthermore, if the electron is liberated from too deep inside the specimen it might never leave the sample or lose the information about its energy or momentum, on its path. Hence understanding the scattering processes and multiple scattering incidence is important to be able to simulate quantitative XPS spectra.

For a more in-depth understanding of the electron interaction processes the reader is referred to [36] and chapter 10 of [20].

These electron scattering processes are the main reason why standard photoelectron spectroscopy is done under ultra high vacuum (UHV), so that the photoelectrons which are excited from the sample are not additionally scattered and thus lose valuable information about the specimen. Since the electrons would be scattered due to their short mean free paths and the additional atoms in the atmosphere. Furthermore the extra atoms of the atmosphere surrounding the sample would quickly contaminate the surface which strongly attenuates the signal from the specimen, then the surface sensitivity of the measurement method results in a disadvantage.

2.1.3 Spectra quantification

XPS is a surface sensitive and precise measurement method which can not only obtain elemental information about an investigated sample but also give relative concentrations and further information about chemical states of the specimen.

Due to the mentioned photoelectric effect (subsection 2.1.1) and this way generated photoelectrons and possible Auger electrons, it is understandable that an XPS spectrum with unique electron energies could be generated. According to the atomic composition of the investigated sample the amount of collected electrons will give different peak intensities from which a relative atomic composition can be calculated. Due to the previously mentioned chemical shift (section 2.1) and the resulting differently shifted peaks the XPS spectrum gives an inside into the chemical states the investigated sample is composed of.

Nevertheless the majority of electrons collected by the detectors will be attenuated and undergo inelastic scattering (subsection 2.1.2) which will result in a background signal. Additional experimental difficulties (e.g. an unmonochromated source, charging effects, contamination etc.) could further distort XPS spectra. Also sample related factors like different ionization cross sections for ionization and surface anomalies would impact the signal. The latter factors are commonly summarised into a relative sensitivity factor S_i (RSF) for quantitative XPS spectrum analysis.

The signal intensity I written as an function of the atomic fraction n:

$$I = n\sigma\theta\lambda AT \tag{2.8}$$

Here the RSF is a product of the factors σ the electron emission cross section, θ equals the angle between the incoming photon beam and the emitting electrons, λ being the photon wavelength, A the photon emission area and T representing the analyser coefficient.

Although when doing chemical quantification usually the main interest focuses on relative concentrations of elements in the investigated sample, which is represented by following equation:

$$\frac{n_i}{n_j} = \frac{I_i}{I_j}\frac{S_j}{S_i}. \tag{2.9}$$

From this the atomic concentration of an specific element C_i is written as:

$$C_i = \frac{I_i/S_i}{\sum_j I_j/S_j}. \tag{2.10}$$

Index $_i$ represents the element of interest whereas the sum over the index $_j$ represents all elements present in the investigated XPS spectrum.

While assumptions are made and these formula (2.8, 2.9, 2.10) might only be valid for plane surfaces with homogenous elemental distributions inside the investigated specimen, it still is a widely used concept giving good approximations within an accuracy of 10%. It must be mentioned that extracting the peak intensities or area from within an experimental XPS spectrum is not trivial since the signal might have additional background components from higher kinetic energy peaks which would need to be subtracted first.

2.1.4 Experimental setup of X-ray photoelectron spectroscopes

As other spectroscopes an XPS apparatus (Figure 2.8) an be divided into three main components: source, sample and analyser or detector.

The source needs to generate X-ray photons since these are the primary probing entities for our XPS device. As mentioned in subsection 2.1.1 the energy values of the photons range between 1-10keV. For typical laboratory equipment soft X-rays (Figure 2.4) are generated by Al-Kα($E_{photon} = 1486.6eV$) or Mg-Kα($E_{photon} = 1253.6eV$) emitters. With the increasing access to synchrotrons and further spectrometer development also hard X-ray photoelectron spectroscopy[5] is done on a regular basis.[37]

[5]Regularly used abbreviations are HXPS, HAXPES or HX-PES

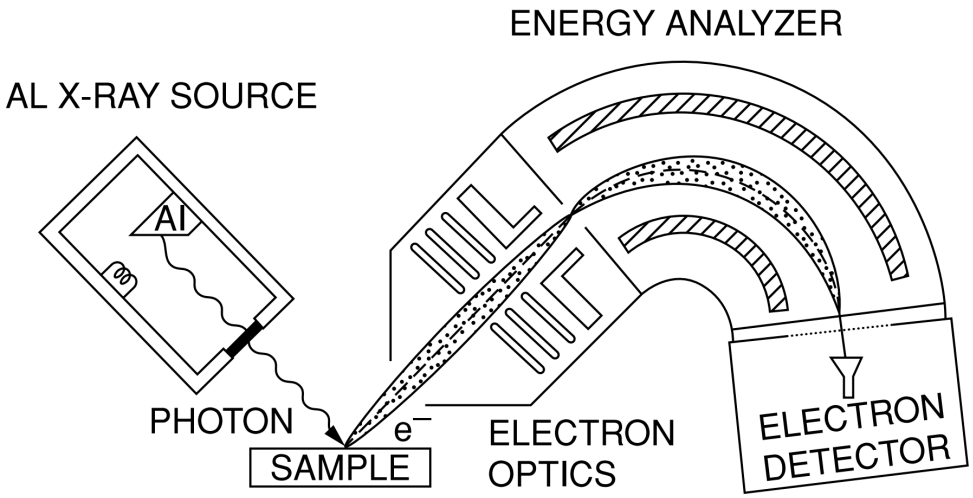

Figure 2.8: Schematic of an XPS apparatus, showing X-ray source an sample and electron optics including a hemispherical mirror analyser and a electron detector. Figure 10.2 taken from reference [19]

The standard approach in generating X-rays is by bombarding a target with electrons. This method was already used by Wilhelm Conrad Röntgen who discovered X-ray photons in 1895 via experiments with Crookes-Hittorf and Lenard tubes.[6]

In an evacuated vacuum tube electrons are forced from a cathode onto a target anode via a field producing a potential difference known as tube voltage or source voltage. The cathode as a thermal source of electrons is usually made from materials with high melting points such as tungsten, molybdenum or lanthanum hexaboride. The created X-ray radiation depends on the anode material, common in XPS are Al and Mg targets. Applied tube voltages accelerating electrons from the cathode to the anode are in the range of several keV. In this way electrons from the cathode knock out inner-shell electrons in the anode material leaving empty states behind which are then refilled by higher state bound electrons accompanied by emission of an energetic X-ray photon. For Al and Mg this produces distinct and intense K_α-lines with energies of $1486.6eV$ and $1253.6eV$, respectively. Important for a precise analysis are sharp photon peaks with a small peak width so that intense and clear photoelectron peaks can be excited and the resulting spectra are clean and undistorted by shadowing effects.

Modern X-ray photoelectron spectroscopes utilize monochromated photon sources to have a higher energy resolution. X-ray monochromators make use of crystalline diffraction and crystalline lattices to focus and select a defined wavelength. This is governed

[6] W.C. Röntgen received the first Nobel Price in 1901 for his discovery of X-Rays.

by Braggs law described by the equation:

$$n\lambda = 2dsin\theta. \tag{2.11}$$

Here two lattice planes with a distance d are hit by incident X-rays with a characteristic wavelength of λ with n being the diffraction order. Now to produce the strongest possible constructive interference a wave has to hit the crystalline lattice under and angle of θ. Such monochromators are not only used to increase the energy resolution of XPS instruments which in return enable detailed analysis of chemical shifts but are also used to improve the experimental lateral resolution of these instruments.

The X-ray production and focus onto a sample is important to be able to probe and investigate a specimen. Inside the sample physical processes take place, transforming photons into electrons mainly through the photoelectric effect (subsection 2.1.1). In this way generated photoelectrons now can further undergo interactions between atoms and electrons inside the specimen (subsection 2.1.2). An overview of the whole process was described in section 2.1.

Eventually electrons might leave the investigated sample and enter the last component of the spectrometer, the analyser. Which again can be divided into three components: electron optics, energy selector and the final electron detector. Giving the analyser the function of collecting the released electrons yielding an X-ray photoelectron spectrum.

Thus XPS and in general photoelectron spectroscopy (PES) setups tend to use electron optics to focus the generated photoelectrons into an analyser. These electron optics utilize electromagnetic fields to manipulate the charged particle beam coming from the specimen into a focus point similar to optical lenses. Although electron optics using magnetic deflections were used most modern laboratory instruments tend to utilize electrostatic lenses nowadays. The manipulation of the moving charged particles due to the electrostatic fields is governed by the Lorentz force.

The two main types of analysers used in PES are cylindrical mirror analysers (CMA) and hemispherical mirror analysers (HMA). While CMAs generally have a higher sensitivity, HMAs deliver a better energy resolution [38, 21]. XPS is relying on spectral resolution for analysing samples and their chemical composition and chemical states thus HMAs are commonly preferred and found on typical laboratory equipment.

The lens system combining the electron optics and the hemispherical analyser can be used in two different modes, the constant analyser energy (CAE) or the constant retard ratio (CRR). The difference is how the pass energy of the lens system is achieved. As the name suggests electrons with this energy can pass trough the analyser on a Kepler orbit. While low pass energies improve energy resolution the signal to noise ratio reduces and consequently a measurement with the same statistics takes longer. For hemispherical analysers the pass energy can be determined by the following equation:

$$E = |e|(V_2 - V_1)(\frac{R_1 R_2}{R_2^2 - R_1^2}) = |e|\Delta V k \tag{2.12}$$

With e being the elementary charge of the electron, V the potential of a hemisphere with R being the hemispheres radius. While the term containing the radii of the hemispheres is a spectrometer specific constant k, the potential difference ΔV can be adjusted by different means. In the constant analyser energy (CAE) mode the analyser is set to specific and constant voltages while sweeping over an energy range to scan a spectrum only the retard voltages of the electron optics are adjusted. In contrast to the CAE mode, in the constant retard ratio (CRR) mode, the retarding voltages of the electron optics are held constant while the analyser scans the spectrum by adjusting its voltage levels on the hemispheres.

In XPS mostly the CAE mode is utilized to collect spectra since it has the property of having a stable energy resolution over the whole scanned energy range of a spectrum. While the CRR mode is often used in Auger electron spectroscopy (AES) due to its higher electron yields and thus enhanced signal to noise ratio.

After the photoelectrons pass the lens system they need to be collected and counted which is usually done by means of electron multipliers. The two most common types of electron multipliers used in current spectrometer setups are channel plates (sometimes referred to as micro-channel plate, MCP) or channel electron multipliers (also known as channeltrons or CEMs). As the name suggests both channeltrons and channel plates are used to multiply the electrons collected, this is done by using coatings of material with high secondary electron yields. When a photoelectron with an energy higher than the material specific threshold energy of the coating hits the multiplier, secondary electrons are generated. This process is multiplied by forcing these secondary electrons further into the multiplier by an applied potential creating a cascade and collecting these secondaries via an anode. Channeltrons are often geometrically shaped like a spiral and can exhibit high signal gains multiplying the input signal by factors of 10^8. Channel plates on the other hand usually are not able to reach as high gains or count rates as channeltrons, but due to their geometrical setup one can detect data in two spatial dimensions. This makes it possible to create XPS setups which are able to detect angle- and energy resolved XPS spectra, or even position dependent electron images.

Further details about the core components can be found in chapter 5 of [20].

2.2 Other electron beam techniques for nanoparticle characterization

This section will give a brief introduction into other electron beam techniques utilized for nanoparticle characterization.

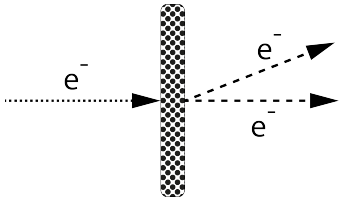

Figure 2.9: Schematic diagram of the process observed via a transmission electron microscope (TEM)

2.2.1 Transmission electron microscopy

Transmission electron microscopy (TEM) is based on a Nobel Prize winning technique developed by Ruska and Knoll in 1931. TEM replaces photons traditionally used for imaging with electrons which increases the theoretical maximal resolution d as per the following equation:

$$d = \frac{\lambda}{2nsin\theta} = \frac{\lambda}{2NA}. \tag{2.13}$$

Where the minimal resolvable distance d is described via Abbes formula for the diffraction limit including the electrons DeBroglie wavelength λ, the mediums refraction index n and the beams half-angle θ. In optical systems $nsin\theta$ is often replaced by the factor NA, the numerical aperture.

As an electron beam is transmitted trough a sample, it gives rise to an image with contrast based on material absorption, thickness and composition of the specimen.

2.2.2 Energy dispersive X-ray spectroscopy

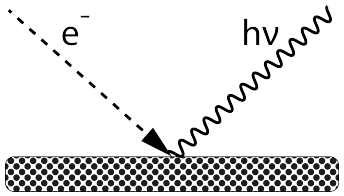

Figure 2.10: Schematic process observed via a energy dispersive X-ray spectroscope (EDS).

As in XPS and Auger electron spectroscopy (AES), in energy dispersive X-ray spectroscopy[7] electrons from inner shells of a sample are excited, leaving an empty state behind. A higher state electron will re-occupy the lower empty state. Due to energy conservation the difference in energy of these states might be released by X-rays. With an energy dispersive spectrometer the emitted photons can be used to characterize the specimen

[7] Commonly used abbreviations are EDX, EDS or EDXS.

and the elemental composition of it. Further details about the process are described in section 2.1.

2.2.3 Electron energy loss spectroscopy

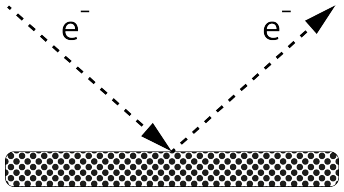

Figure 2.11: Schematic diagram describing the process in an electron energy loss spectroscope (EELS).

Developed in 1944 by Hiller and Baker electron energy loss spectroscopy (EELS) is also referred to as a complementary technique to EDX, as EELS tends to have a better energy resolution. The specimen is exposed to an electron beam with primary probing electrons undergoing inelastic scattering an thus loosing energy through interaction processes in the sample. Analysing the electrons' energies via a spectrometer gives insight in the undergone processes and sample composition. In the high loss part of the electron energy loss spectrum characteristic ionisation edges are found, which hold information about the sample chemistry. Different types of EELS exist based on the geometry of the spectrometer, such as reflection (REELS) or transmission (TEELS) giving them unique properties for investigating specific processes such as plasmons or band structure analysis.

The main differences these electron beam techniques have compared to XPS are the probing particles. EDX, EELS and TEM are using electrons with energies from 100-300keV whereas XPS is using photons with energies around 1-10keV. Giving the photons the ability to penetrate into the specimen much deeper into the sample due to the missing electric charge of the probing particles.

3 Models for electron transport in electron spectroscopy

Simulating electron transport is very important for the quantitative interpretation of XPS spectra, in particular for complex morphologies such as core-shell nanoparticles (CSNP). For the simulations some approximations are made, in the quasi-elastic approximation (QEA) the energy dependence of the inelastic interaction characteristics are neglected. Although it is a very good approximation and even exact for the elastic component the true slowing down (SDN) algorithm is more realistic. To combine the accuracy of SDN with the speed of QEA another enhanced version QEA+ was tested and further refined into QEA*.

The purpose of this chapter is to give a short overview of the currently utilized approach in SESSA for simulating spectra and the main differences to the newly implemented true slowing down (SDN) algorithm.

Additionally further improvements of the mentioned methods will be discussed, leading to physically more accurate simulated spectra.

Some models for quantifying XPS signals from CSNP are discussed and compared at the end of this chapter. The majority of these models take into account the signal peak intensities but disregard the majority of the collected electrons in the spectrum background shape. Problems arising from this information limitation are shortly touched at the end of this chapter.

3.1 SESSA

Quantifying simple geometries of planar samples in specific experimental setups can - under circumstances - be calculated by hand, but this task gets difficult very quickly. Special experimental geometric setups with complex sample morphologies and chemical composite materials illuminated by polarized X-ray photons will increase the difficulty of this task into a lifetimes work.

For this purpose *Simulation of Electron Spectra for Surface Analysis* (SESSA) [39, 40] which is distributed by the *National Institude of Standards and Technology* (NIST) and developed in cooperation by the research group *Surface and Plasma Technology* of the *Institute of Applied Physics* at the *Vienna University of Technology* is the perfect tool. It is a database software for simulating quantitative XPS and AES spectra. As of Version

2.0 the PENGEOM package from the *Penetration and ENErgy LOss of Positrons and Electrons* (PENELOPE) [41, 42] code system was included into SESSA which enables spectrum simulations of arbitrary sample morphologies by constructing quadric surfaces of the investigated morphology. With Version 2.1 the ability to load externally created user defined geometries into SESSA was added.

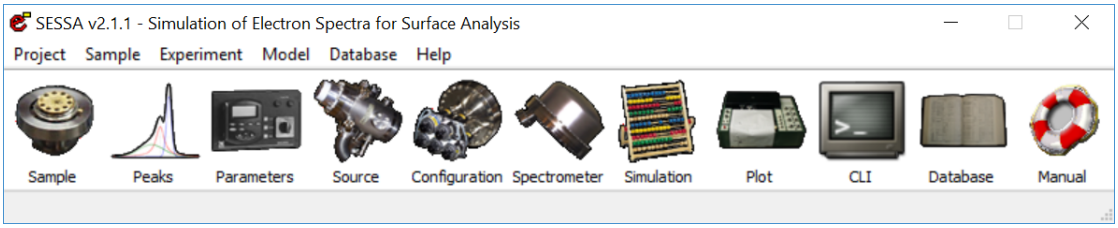

Figure 3.1: Main user interface of *SESSA v2.1.1*.

In order to generate a simulated spectrum with SESSA one must first input all relevant parameters: the source energy and type, the experimental geometries describing the orientation of the sample surface normal, the source and analyser axis with the aperture opening angles and possible polarization vectors. Further input parameters are the spectrometer energy range and sample morphology and the material composition.

The parameter input can be done via a graphical user interface (Figure 3.1), an additional command line interface or by loading text based session files which could be generated or written manually.

With these parameters SESSA gets the necessary variables via its expert system from the built-in databases. According to the selected model it then creates the requested spectrum by the built in Monte Carlo method.

A detailed usage description can be found in the SESSA user guide [39].

3.1.1 Quasi-elastic approximation

SESSA utilizes the quasi-elastic approximation (QEA) [43] which assumes that the typical occurring electron energy losses ΔE are small compared to the initial kinetic energies E_0 in the medium energy range ($E_0 \gtrsim 200eV$). These Energy losses are typically in the order of about one Hartree (or two Rydberg).

$$E_0 >> \Delta E \sim e^2/a_0 = 27.2eV \sim E_h = 2Ry \tag{3.1}$$

With e being the elementary charge and a_0 Bohrs radius.

Within the QEA, the energy dependence of the interaction characteristics such as the mean free paths λ are neglected.

$$\lambda_n = \lambda(E_n) \approx \lambda(\overline{E}_n) \tag{3.2}$$

Index n is the number of occurred scattering events with $\overline{E}_n$ being the average energy after n inelastic collisions.

As mentioned in section 3.1, SESSA is able to simulate an XPS or AES spectrum based on user input. The calculation takes advantage of the partial intensity approach (PIA) [44] which is based on the assumption that the spectrum can be separated into two independent functions with an energy- and an angle-dependent part. This assumption is based on the argument that elastic and inelastic scattering could be viewed as separate events, because for elastic scattering mostly the changes of the projectile scattering angle are relevant and the energy losses are negligible and vice versa for inelastic scattering processes. This behaviour is rooted in the mass difference of projectile (the electron) and target (the ionic cores).

With this approach the spectrum can then be written as a weighted superposition of energy distributions from groups of electrons that have experienced n inelastic collisions:

$$Y(E,\vec{\Omega}) = \sum_{n=0}^{N_{max}} F_n(E) C_n(\vec{\Omega}) \tag{3.3}$$

The spectrum $Y(E,\vec{\Omega})$ is calculated as the sum over the product of the partial intensities $C_n(\vec{\Omega})$ i.e. the number of electrons that participated in n inelastic collisions and the partial energy distributions $F_n(E)$ being their corresponding energy distributions. N_{max} is the maximum number of interactions that needs to be taken into account for the considered energy range. [39]

Here the partial energy distribution after n inelastic collisions is the energy dependent part of the equation.

$$F_n(E) = \int L_n(T) f_0(E+T) dT = \int F_{n-1}(E+T) w(T) dT \tag{3.4}$$

It can be described as a convolution of the partial loss distribution $L_n(T)$ with the normalized source energy distribution $f_0(E)$. Alternative description is a self convolution of the previous $F_{n-1}(E+T)$ partial energy distribution after $n-1$ inelastic collisions with the normalized inverse inelastic mean free path (nDIIMFP) $w(T)$, for all occurred energy losses T. [36, 39]

The partial loss distributions $L_n(T)$ (used in Equation 3.4) are described by:

$$\begin{aligned} L_0(T) &= \delta(T) \\ n \geq 1 : L_n(T) &= \int L_{n-1}(T+T') w(T') dT' \end{aligned} \tag{3.5}$$

These quantities describe the distribution of energy losses after n inelastic collisions and are given in Equation 3.5 as a recursive self convolution of the normalized differential inverse inelastic mean free path (nDIIMFP) $w(T')$ for a specified energy loss T'. The

zero order distribution $L_{n=0}$ represents the elastic peak and is given by a delta function. [45, 44, 36]

The normalized differential inverse inelastic mean free path (nDIIMFP) in the QEA is energy independent and defined as:

$$w(T) \approx w(T,E) = W(T,E)\lambda_i, \tag{3.6}$$

were $\lambda_i(E) = [\int_0^\infty W(T,E)dT]^{-1}$ is the inelastic mean free path (IMFP, Figure 3.2) and $W(T,E)$ the differential inverse inelastic mean free path (DIIMFP). The DIIMFP is related to the dielectric constant of a material $\epsilon(q,T)$ and for inelastic scattering event inside a bulk material $W_b(T,E)$ defined as [36]:

$$W_b(T,E) = \frac{1}{\pi a_0 E}\int \frac{dq}{q} Im\frac{-1}{\epsilon(q,T)}. \tag{3.7}$$

Here E represents the electrons energy and q the transferred momentum.

Both the zero order source energy distribution $f_0(E)$ and the differential inverse inelastic mean free path $w(T)$ are normalized and per definition equal to unity:

$$\left.\begin{aligned}\int f_0(E)dE\\ \int w_0(T)dT\end{aligned}\right\} \equiv 1. \tag{3.8}$$

Consequently both the partial energy distribution $F_n(E)$ and the partial loss distributions $L_n(T)$ with the index n representing the amount of undergone inelastic collisions are normalized too.

The second factor forming a spectrum (Equation 3.3) is the partial intensity described by:

$$C_n(\vec{\Omega}) = \int Q(s,\vec{\Omega})W_n(s)ds \tag{3.9}$$

Which is calculated as a convolution between the path length distribution $Q(s,\vec{\Omega})$ and the probability for n-fold scattering $W_n(s)$. Where s is the path length and $\vec{\Omega}$ represents the electron emission direction. [46, 36]

The applied quasi-elastic approximation leads to the simplification that the probability for n-fold scattering $W_n(s)$ as a function of path length s becomes equal to the Poisson distribution. [47, 46]

$$W_n^{QE}(s) = P_n(s/\lambda) = \left(\frac{s}{\lambda}\right)^n \frac{e^{-s/\lambda}}{n!} \tag{3.10}$$

For further improvement of the calculation speed the trajectory reversal method (TRM) [48, 36] is applied. This method is possible only within the QEA, because the energy

dependence of the inelastic scattering events are neglected the electrons paths can be calculated in the reverse direction. Since in the quasi-elastic approximation the reverse direction trajectories are equal to the forward calculated trajectories. All the calculated paths start in the final destination, the detector, therefore only collected electron trajectories are calculated.

For a more detailed description of the utilized approaches and approximations the reader is referred to [39] and [36].

3.1.2 True slowing down method

For this work, the simulation models in SESSA (see section 3.1) were enhanced by implementing an additional method, the true slowing down (SDN) algorithm which models the electrons path out of the sample including elastic and inelastic scattering, fully taking into account the energy losses which occur during the inelastic incidents and the concomitant change of the cross sections. This adds the ability to use IMFP values according to the material the electron is travelling through including the corresponding electron energy, resulting in the usage of physically more accurate IMFP values used for each inelastic scattering event.

This comes at a cost of computation time, mainly because the reverse trajectory approximation (TRM) cannot be utilized anymore. This is due to the fact that each electrons path through the sample has to be modelled in the traditional forward manner to fulfil the energy conservation law.

Due to the forward trajectory simulation many more electron paths and scattering events have to be calculated because the emission angles are nearly isotropic and thus we will end up simulating electron paths which actually don't end up in the detector and thus do not contribute to the simulated spectrum.

3.1.3 Beyond the quasi-elastic approximation

The previously discussed QEA model, which is currently used as the default simulation model in SESSA, has the benefit of being able to compute a spectrum for a given physical sample in a short amount of time - typically within seconds or minutes. However the used quasi-elastic approximation might not be valid over the wide energy range a spectrum is simulated for. Thus creating the need for a more accurate description, as produced by the true slowing down (SDN) method. As mentioned the SDN method has a downside as it is far more costly in terms of computation time compared to the quasi-elastic approximation (QEA).

Certainly both benefits, the fast computation of the QEA and the more accurate full spectrum of the SDN method in one model would be convenient. Combining both characteristics might work by using the QEA as a base calculation and normalizing the whole spectrum with the overall IMFP energy dependence.

Let $Y_{QEA}(E)$ be the spectrum calculated in the quasi-elastic approximation, then the spectrum $Y_{QEA+}(E)$ should approximately account for the energy dependence of the inelastic electron interactions, as follows:

$$Y_{QEA+}(E) = Y_{QEA}(E)\frac{\lambda(E)}{\lambda(E_0)} \simeq Y_{QEA}(E)\left(\frac{E}{E_0}\right)^{0.7}. \tag{3.11}$$

Here Y_{QEA} is the yield representing the whole simulated spectrum multiplying each intensity by the energy dependency of the inelastic mean free path, starting from and normalizing it to the highest energetic elastic peak E_0. With $\lambda(E)$ being the inelastic mean free path (IMFP) for a specific energy E. The approximation to represent the IMFP function as a function $x^{0.7}$ is only only valid above the minimum of the IMFP function, which is usually around $100eV$. Since the IMFP functions behaviour changes significantly over the whole energy range as visualized in Figure 3.2.

This approximation of the IMFP energy dependency above kinetic energies of around $100eV$ is based on the simple equation $\lambda = kE^m$ described in the work by Seah and Dench [49], which was revised by Wagner et al. [50] with later work by Tanuma et al. [51] showing a good overall agreement for values of $k \sim 0.1$ and $m \sim 0.77$.

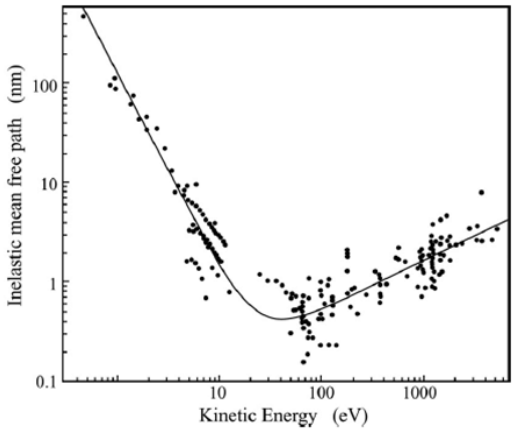

Figure 3.2: Universal IMFP curve proposed by Seah and Dench showing the inelastic mean free path of electrons in nm against the kinetic energy in eV, adapted from [49]

As a conjecture for further improving the quality of the approximation, simulations were done where the energy dependence approximation $x^{0.7}$ was not applied to the final Y_{QEA} spectrum but before summing the whole spectrum together to the single peak spectra which it consists of. This further enhancement is referred to as $QEA*$.

$$Y_{QEA*}(E) = \sum_{j}^{peaks} Y_{j(QEA)}(E)\left(\frac{E}{E_0}\right)^{0.7} \tag{3.12}$$

This improves the validity of the calculated peak intensities since when a spectrum consists of more than one peak, which is usually the case, in the $QEA+$ approximation peaks at lower energies would be also weighted by the normalization factor $(E/E_0)^{0.7}$ and therefore be obscured by it. But when the normalization factor is applied to each single peak spectrum before adding it together to the final spectrum only the inelastic XPS backgrounds are corrected and the elastic peak intensities are not manipulated.

3.2 Quantifying core-shell nanoparticles

Quantification of layer thicknesses for planar specimens by means of XPS is done by interpreting ratios of peak intensities or by additional measurement methods like angle resolved XPS (ARXPS) [52]. While these methods come with their own challenges and uncertainties they do not take into account the details of a sample morphology. Therefore quantification methods for complex sample morphologies such as core-shell nanoscopic spheres were developed. Shards straightforward method [16] for interpreting XPS data determines shell thicknesses for ideal core-shell nanoparticles based on peak intensities with high accuracy. With the infinitesimal columns model [17] XPS peak intensities for core-shell spheres and core-shell-shell spheres can be calculated and compared with experimental data giving a best fit for the expected corresponding shell thicknesses. The same method can be utilized with SESSA which simulates XPS data for arbitrary sample morphologies, and are later compared with experimental data. For core-shell nanoparticles SESSAs model and Shards T_{NP} equation were compared in reference [53] showing good agreement between these two models. Tougaard showed that neglecting the XPS background essential information about the sample morphology could be lost and peak intensities are not unique. [18]

3.2.1 Shards model

Since the dimension and shell thickness of core-shell nanoparticles are very important parameters of such samples a direct evaluation method of XPS spectra would be very valuable. In Reference [16] development of such a method by numerical calculations and parameter fitting procedures is described. Important boundary conditions for the validity of this methods' findings are first of all that ideal concentric core-shell structures are being used in the experiment and that elastic scattering of electrons is neglected or in other words the straight line approximation is employed.

The method proposed by Shard [16] uses the dimensionless ratio A of normalized shell

intensities I_s/I_s^∞ to core intensities I_c/I_c^∞ which is defined as:

$$A = \frac{I_s I_c^\infty}{I_c I_s^\infty}. \tag{3.13}$$

Here the I_i is the intensity from a measured XPS spectrum and I_i^∞ the intensity for the same material with infinite thickness.

Further dimensionless ratios are the normalized electron attenuation lengths $L_{i,j}$ which are defined as,

$$B = \frac{L_{s,s}}{L_{c,s}}, C = \frac{L_{s,s}}{L_{s,c}}. \tag{3.14}$$

The first index i defines which material the photoelectron is originating from while the second index j specifies which material the electron is travelling through. The index s represents the shell and the index c the core resulting in $L_{s,s}$ the shell-shell photoelectron attenuation length.

The first step to generating a simple and direct formula was the adaption of the "Thickogram" equation from [54] by limiting the extreme values and reformulating it to a planar thickness equation,

$$T_{planar} = \frac{A^{2.2} \ln AB^{-0.95} + 2AB^{-0.42}}{A^{2.2} + 1.9}. \tag{3.15}$$

By a combination of numerical calculations, variations and factor weighting Equation 3.15 was found. The essential outcome here is that it is possible to convert XPS data directly to thicknesses within some boundary conditions.

Since the surface of very large spheres can be viewed as planar, a variation of T_{planar} was refined with a correction term, the so called "Topofactor" [55]. With some further optimization the thickness equation for microscopic spherical particles $T_{R\to\infty}$ with radii much larger than one shell-shell photoelectron attenuation length but less than $\sim 1000 L_{s,s}$ - so that X-ray shadowing effects are not yet of significance - was found to be,

$$T_{R\to\infty} = \frac{0.74A^{3.6} \ln AB^{-0.9} + 4.2AB^{-0.41}}{A^{3.6} + 8.9}, \tag{3.16}$$

to follow a similar procedure as for finding the T_{planar} equation. Narrowing down to a straightforward equation for nanoparticles the other extreme in contrast to the $T_{R\to\infty}$ for infinitesimal small particles was obtained by the equation,

$$T_0 = R[(ABC + 1)^{1/3} - 1]. \tag{3.17}$$

With R being the core radius of the particle in units of the shell-shell electron attenuation length $L_{s,s}$, the same units as those used for the shell thicknesses T.

Further investigation of $T_{R\to\infty}$ and T_0 with factor variations and numerical calculations revealed that for nanoparticle sizes of $\sim 2.5nm$ up to $\sim 160nm$ the following equation

$$T_{NP} = \frac{\frac{T_{R\to\infty} R}{R+\alpha} + \beta T_0}{1 + \beta}, \tag{3.18}$$

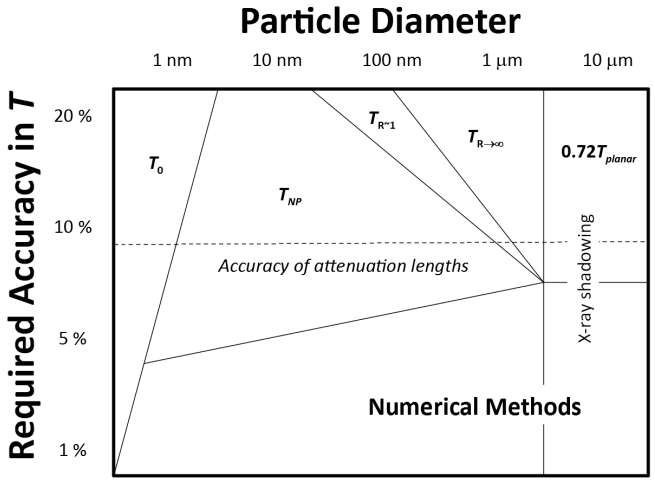

Figure 3.3: Accuracies of Shard equations including accuracy of attenuation length for different particle diameters, for exact quantitative analysis numerical methods need to be employed. For overlayer thicknesses in the μm range X-ray shadowing will occur. Figure 6 from [16].

will give very accurate shell thickness estimations with a mean error of approximately 4%. This is excellent when compared to the general error estimations of attenuation lengths which is reported to be around 10%, see Figure 3.3. [56]

The weight factors,

$$\alpha = \frac{1.8}{A^{0.1}B^{0.5}C^{0.4}}, \tag{3.19}$$

$$\beta = \frac{1.3\alpha^{2.5}}{R^{1.5}}, \tag{3.20}$$

expand the range in which Equation 3.18 is valid for different values of R.

With Equation 3.18 a major step towards easy and direct use of XPS data for shell thickness determination was established. The equation depends on normalized relative shell to core peak intensities which can be found in an XPS spectrum and material specific attenuation lengths, revealing accurate shell thickness estimations for a wide range of CSNP diameters. It should be kept in mind that this method was brought up on two important simplifications and model assumptions. First the straight line approximation (SLA) was used neglecting scattering effects and second it's developed for ideal nanoparticles with core and one shell morphology.

For details the reader is referred to the original work by Shard, [16].

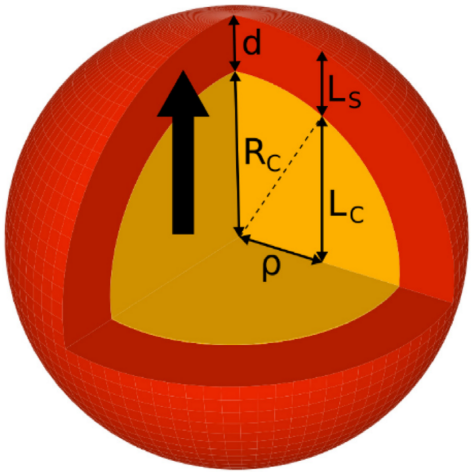

Figure 3.4: For the IC model the investigated CSNP are divided into columns with corresponding variable definitions, figure 1 from [17]

3.2.2 Infinitesimal Columns model

Another model to determine shell thicknesses of CSNP by XPS analysis is the "Infinitesimal Columns" (IC) model described in [17]. Similar to the previous model, intensity ratios based on the "Thickogram" [54] equations are the starting point for this model. The signal intensities are assumed to follow Equation 2.3 and depend on the inelastic mean free path (IMFP). Analogous to the previous model the energy dependency is neglected and the straight line approximation (SLA) is applied.

The particle is divided into infinitesimal columns, each consisting in part of a core L_C and a shell L_S layer depending on the columns distance to the particle centre (see Figure 3.4):

$$L_C(\rho) = \sqrt{R_C^2 - \rho^2}, \tag{3.21}$$

$$L_S(\rho) = \sqrt{(R_C + d)^2 - \rho^2} - L_C. \tag{3.22}$$

Each of these infinitesimal columns contributes with an intensity (i_C, i_S):

$$i_C(\rho) = X_C \cdot \lambda_{Cc} \cdot (1 - e^{-2L_C(\rho)/\lambda_{Cc}}) \cdot e^{-L_S(\rho)/\lambda_{Sc}}, \tag{3.23}$$

$$i_S(\rho) = X_S \cdot \lambda_{Ss} \cdot (1 - e^{-L_S(\rho)/\lambda_{Ss}}) \cdot (1 + e^{-2L_C(\rho)/\lambda_{Cs} - L_S(\rho)/\lambda_{Ss}}), \tag{3.24}$$

to the total signal:

$$I_{C,S} = 2\pi \int_0^{R_C - d} \rho \cdot i_{C,S}(\rho) d\rho. \tag{3.25}$$

For an actual shell thickness determination from an experimental XPS spectrum, signal intensity ratios I_S/I_C need to be calculated and compared between simulated and ex-

perimental data yielding the best match for the estimated shell thickness. Error ranges for the thickness estimations are reported to be in the range of around 10% .

In contrast to the T_{NP} formula one can define further layers and add their contributions to the total signal intensity. Giving the model the ability to account for other morphologies, although the equations need to be adjusted and the calculations need to be re-done.

With the feature of taking into account different morphologies the IC model loses the ability to simply and directly evaluation XPS spectra which the T_{NP} equation offers.

For a detailed information about the IC model definitions, refer to [17].

3.2.3 SESSA model comparison

In reference [53], simulated XPS spectra created by SESSA with shell thickness estimations by Shards T_{NP} formula were evaluated. Figure 3.5 shows a comparison of four different ideally shaped spherical core-shell nanoparticles with different core sizes I-IV. For the assumed thickness value T_{SESSA} as the simulated XPS data is compared to the reproduced values by the T_{NP} formula, both in units of shell-shell electron attenuation length. Two extreme cases are taken into account, Be on Au representing the case of a light shell element wrapped around a heavy element in the core. The second sample Pd on Al_2O_3 being the opposite case with an heavy element shell and a light element material in the core. For both cases the straight line approximation (SLA) reproduced nearly a perfect fit and would therefore yield the correct values of shell thicknesses. However when elastic scattering events are taken into account a systematic error is visible for CSNP with heavy elements in the shell. This is expected since for heavy elements electrons are more probable to scatter elastically in this layer.

Furthermore the SESSA simulated spectra were compared to measured experimental spectra which showed a good overall agreement between the simulated peak intensities and experimental peak intensities. Even for full spectra - including the inelastic background - the comparison showed promising results and visible differences for unique morphologies could be simulated.

This work validates SESSAs model by comparison to Shards model and promises the ability to include morphologies into the simulation. For additional information refer to [53].

3.2.4 XPS background

As mentioned most XPS quantification methods are based on peak intensities and comparison of unique peak signals originating from different materials inside a sample. However Tougaard showed that the inelastic backgrounds of the XPS spectra might be an

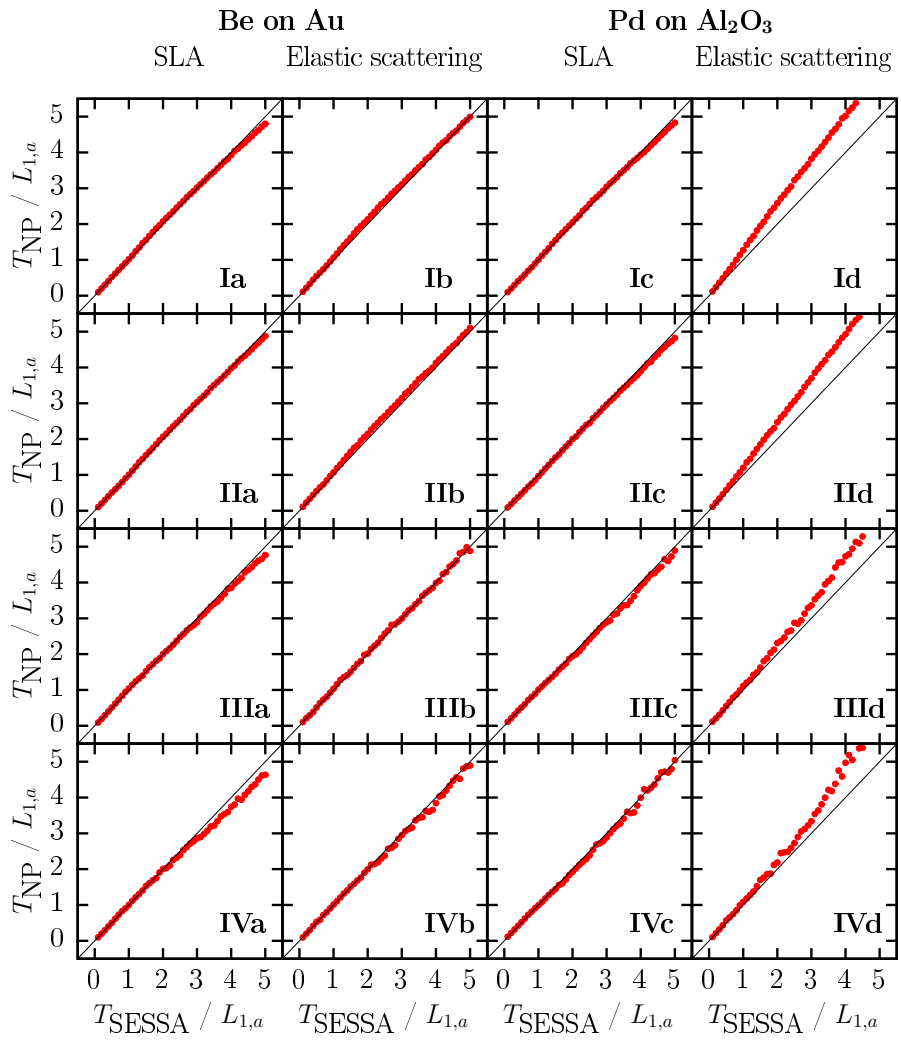

Figure 3.5: Model comparison of T_{SESSA} and T_{NP} in units of shell-shell electron attenuation Length $L_{1,a} = L_{S,S}$ for different CSNP size with respective core radii: $R_I = 32L_{S,S}$, $R_{II} = 8L_{S,S}$, $R_{III} = L_{S,S}$, $R_{IV} = 0.5L_{S,S}$, figure 2 from [53].

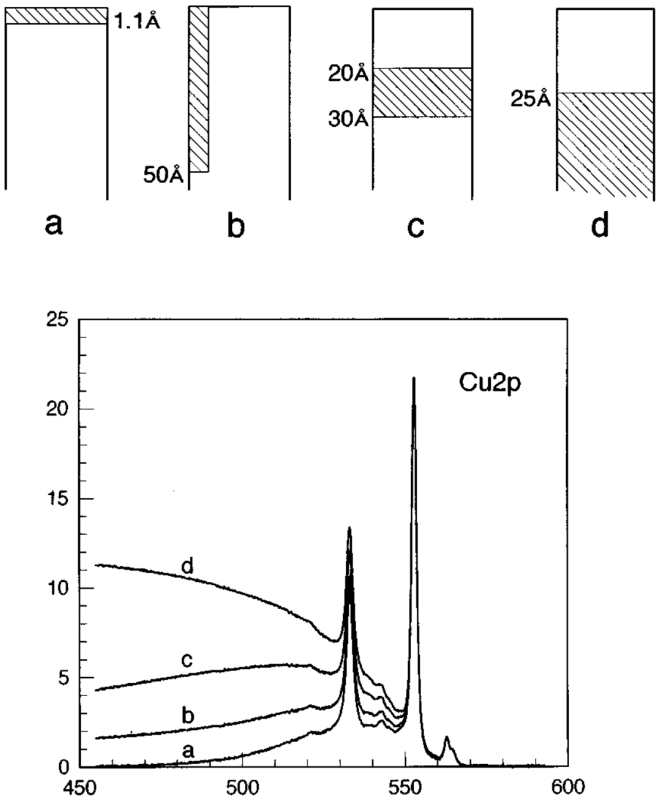

Figure 3.6: Different sample structures resulting in unique XPS background shapes although the peak intensities are identical, figure 1 from [18].

additional and useful analytic tool which could be utilized to get a deeper understanding of an investigated sample and its morphology or structure [18].

Figure 3.6 illustrates four different geometrical morphologies of copper in a gold matrix, Tougaard was able to show that the peak intensities for the $Cu2p$ peaks are identical although the structures differ significantly in material distribution. However the background signals show clear distinctions between the different sample morphologies.

Concluding that the peak intensities are not unique to different morphologies and if taken solely into consideration quantification errors would be huge. Also showing that the background signal is adding valuable information about depth and location of the material constituents, with a general trend of background signals being more intense when electrons are created in layers deeper inside the sample.

A more accurate quantification based on the whole XPS spectrum can be made and quantification methods should be taking into account the background signal information when determining sample morphologies from XPS data.

However, Shard noted in reference [16] that this method might only be practical for

particle sizes of above $\sim 10nm$ or shell thicknesses of above ~ 3 photoelectron attenuation length. Since only then enough inelastic electron collisions might occur for a significant change of the signal.

Nevertheless, accurately simulating the whole XPS spectrum including the inelastic background will help with interpretation of experimental data. Here the benefit of SESSA being able to simulate whole XPS spectra for arbitrary sample morphologies will help when comparing simulated spectra with experimental data, adjusting and testing structural and morphologic sample variations to generate a perfect data fit.

4 Application to spectra from nanoparticles

This chapter introduces the investigated core-shell nanoparticles (CSNP), HM3 which are composed of a polymethylmethacrylate shell with a polytetrafluoroethylene core. Through combination of different electron microscopy techniques common features of the investigated HM3 particles were observed, the vast majority of particles showed acentric cores with strong varying shell thicknesses. These experimentally observed irregularities in the investigated CSNP were also dealt with in XPS simulations. Furthermore a comparison of the newly implemented simulation methods in SESSA, the true slowing down algorithm (SDN) and the enhanced quasi-elastic approximation (QEA+), are given.

4.1 Sample description of HM3

The investigated CSNP sample (HM3) was provided by the Innanopart project partner *University of Eastern Piedmont Amedeo Avogadro (PMO)*. PMO manufactured the samples via the seeded emulsion polymerization process where polytetrafluoroethylene (PTFE) seeds[1] supplied by *Solvay Specialty Polymers*[2] were coated with methylmethacrylate (after polymerization polymethylmethacrylate, PMMA). As process initiator potassium persulfate (KPS) was used. This process produces core-shell nanoparticles with a PTFE core and a PMMA shell, in short PTFE@PMMA.

PMO used SEM images of the seed particles to verify a $47nm$ diameter with a standard deviation of $8nm$. The same method was used after the polymerization process to get a value of $56nm$ particle diameter with a $6nm$ standard deviation for the HM3 samples. Subtracting those two average diameters resulted in the estimated shell thickness of $4.5nm$. Although later work showed a bigger reference value of about $7nm$ for the shell thickness, as reported in the project deliverable D6 and in reference [57].

For PMOs measurement details the reader is referred to the appendix, where the data sheet **Samples WP3** is attached.

The core material PTFE can be described by the chemical formula $(C_2F_4)_n$, commonly referred to as Teflon. The chemical formula describing the shell material PMMA is

[1] https://www.solvay.com/en/products/brands/hyflon-ad
[2] Rue de Ransbeek 310, 1120 Bruessels, Belgium

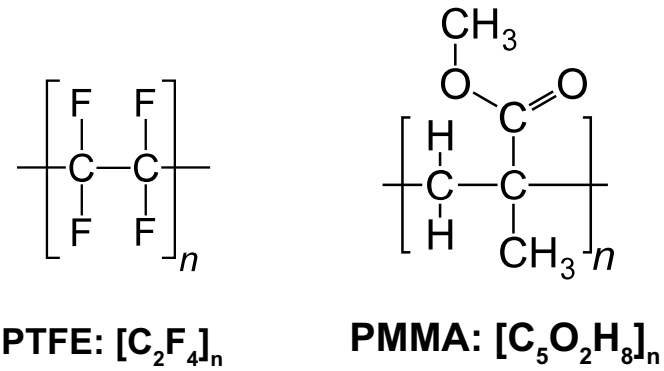

Figure 4.1: Chemical and structural formulae of shell material PMMA and core material PTFE used in the investigated HM3 sample particles.

$(C_5O_2H_8)_n$, common names are Plexiglas, Perspex or Crylux. Both chemical structures can be found in Figure 4.1. For the PTFE material fluorine is always in the same chemical structure and therefore an XPS peak consisting of only one component is expected and visualized in the left detailed XPS scan shown in Figure 4.2 with the single component peak at a binding energy of around $689.5eV$. The right spectrum visible in Figure 4.2 is representing the carbon $C1s$ XPS peak, according to the chemical structure is also expected to be composed of only one single peak at a binding energy of around $292.5eV$.

PMMA as represented on the right hand side of Figure 4.1 has a much more complex chemical structure, unique to the elements of this material are hydrogen (H) and oxygen (O). Since hydrogen (H) is not detectable with XPS, oxygen (O) is a clear choice representing the shell material. The detailed XPS scan on the right hand side of Figure 4.3 shows that the $O1s$ peak is composed of two components with binding energies of around $532eV$ and $\sim 534eV$, respectively. This is expected as the chemical environments of the oxygen atoms in the PMMA molecule differ. Due to the complex chemical structure of PMMA the carbon peak $C1s$ for the shell material PMMA splits into four different components, since the different carbon atoms in the molecule encounters unique chemical environments and thus experience according distinct energy shifts as represented in the left detailed XPS spectrum of Figure 4.3.

Since the two elements fluorine (F) and oxygen (O) are unique features of the core and the shell respectively, one can already determine the signals origin for those XPS peaks. Another possibility is the use of the carbon $C1s$ peak of PTFE and the corresponding chemically shifted components of PMMA for the signal origin distinction. However, due to the close energy proximity the peak intensity determination from experimental spectra of the distinct components might introduce an error.

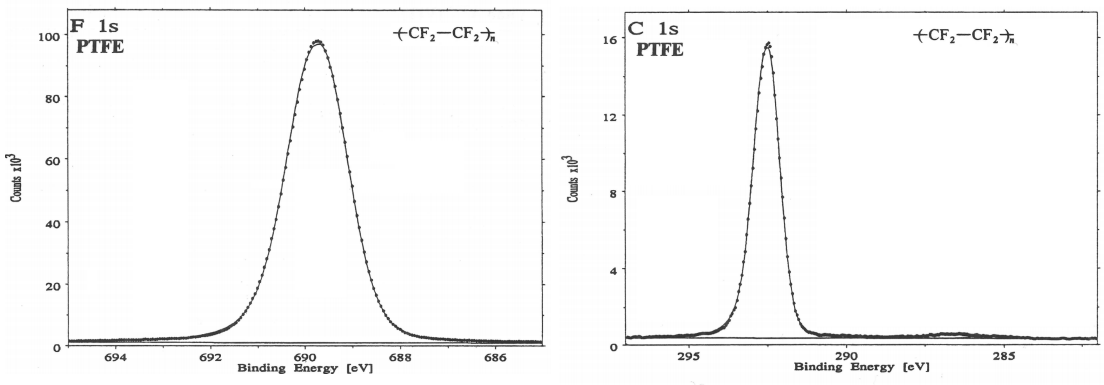

Figure 4.2: Left spectrum showing the PTFE XPS peak for the $F1s$ signal at a binding energy of around $689.67eV$. Right spectrum shows the $C1s$ peak for PTFE at a binding energy of around $292.48eV$. Adapted from [29] page 230 and following.

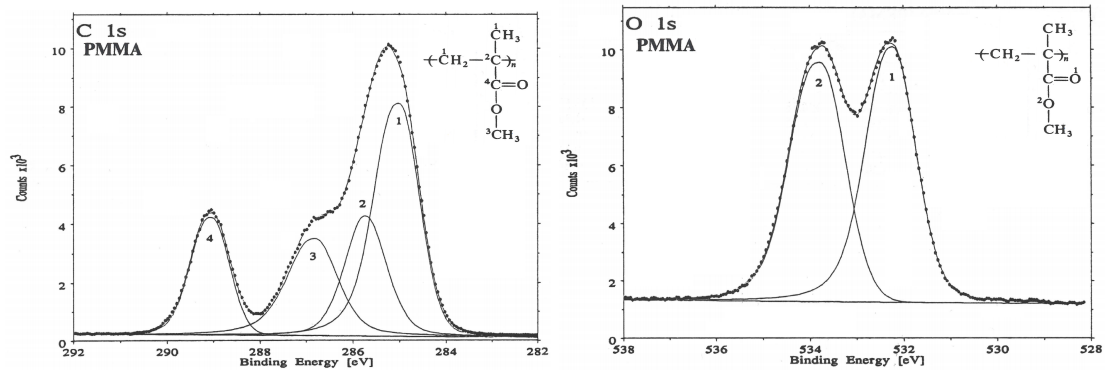

Figure 4.3: Left spectrum shows PMMAs $C1s$ peaks with their different chemical shifts at binding energies of around $285eV$, $285.72eV$, $286.79eV$ and $289.03eV$. Right spectrum shows the $O1s$ components of PMMA at binding energies of around $532.21eV$ and $533.77eV$. Adapted from [29] page 188 and following.

4.2 XPS analysis of HM3 core-shell nanoparticles

Part of the assignments within the Innanopart project was the shell thickness determination via XPS quantitative analysis methods of mentioned PTFE@PMMA core-shell nanoparticles, HM3. For this purpose in a small inter-lab study XPS spectra were taken and compared between the project parters from BAM (Berlin, Germany), NPL (Teddington, United Kingdom) and TUW (Vienna, Austria).

Figure 4.5 shows the full XPS spectrum taken at TU Wien utilizing the available X-ray photoelectron spectroscope which was custom-build by the company SPECS Surface Nano Analysis GmbH[3]. It is equipped with a SPECS μFocus 350 small-spot X-ray source and a PHOIBOS 150 WAL (wide-angle lense) hemispherical analyser. The analysers wide angle lens system has a polar opening angle of $\pm 30°$ and an azimuthal opening angle of $\pm 3.75°$ with respect to the centre of the opening slit. The taken XPS spectra were recorded at pressures below $3 * 10^{-9}$mbar using monochromated $AlK\alpha$ X-rays with an analysis spot of approximately $400\mu m$. To calibrate the instruments energy scale the position of the aliphatic $C1s$ peak was adjusted to the binding energy of $285.0eV$. As mentioned in subsection 2.1.1 charge compensation needs to be considered for these insulating organic particles. For this purpose a low-energy electron flood gun was used at $5V$ with a current of $25\mu A$.

As for the geometrical setup of this XPS experiment, the orientation of the X-ray source is at a polar angle of 30° with respect to the sample surface normal. The analyser is set at a polar angle of 51° with respect to the sample surface normal and an azimuthal angle of 90° with respect to the X-ray source. The resulting angle between source, sample and analyser is approximately 55° which is close to the so-called magic angle.

The sample preparation is tedious but of great importance for a surface sensitive method like XPS. In previous work [57] different preparation methods were performed and reviewed. For the XPS measurements at the TU Wien undiluted and diluted versions of the suspensions were prepared as visible in Figure 4.4. In the deposition process latex gloves were worn to minimize surface contamination and exposure. A purified silicon (Si) wafer was prepared via a $10min$ sonication in ethanol with a followed up drying under nitrogen. The undiluted core-shell nanoparticle liquid suspension was deposited onto the cleaned Si wafer via drop casting $3\mu l$ drops from a $10\mu l$ capacity pipette. As this experimental XPS setup requires dry solid specimen and to speed up the preparation time the Si substrate was dried in a vacuum desiccator. The process of drop casting with following drying was repeated several times until a homogeneously distributed solid was formed. The drying process needed to be performed after each drop to be able to place the following drop in the centre of the previous one.

Additionally to the undiluted specimen a $1 : 99$ dilution with distilled water of the HM3 core-shell nanoparticle suspension was prepared. As in the undiluted case the silicon

[3]SPECS Surface nano Analysis GmbH, Voltastrasse 5, 13355 Berlin, Germany. http://www.specs-group.com

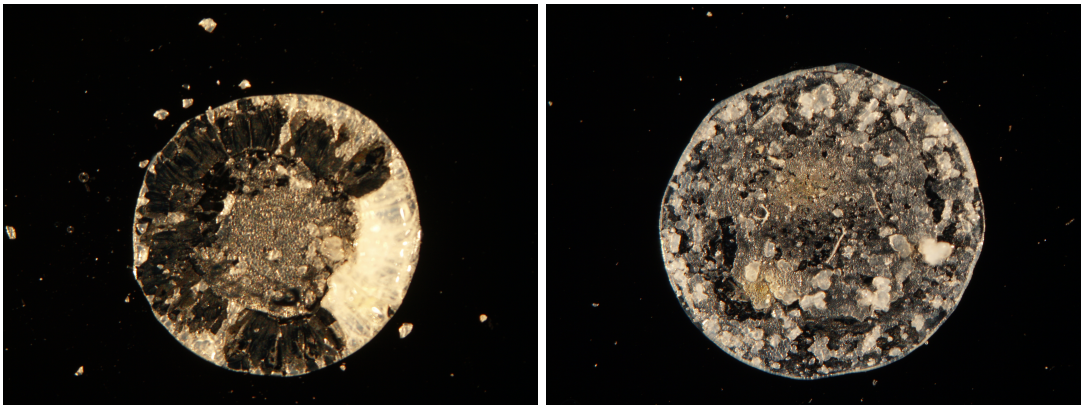

Figure 4.4: Two optical microscopy images of differently prepared HM3 core-shell nanoparticle sample spots for XPS analysis. Both spots are $3mm$ wide in diameter. The left image shows a spot prepared from the undiluted HM3 suspension. On the right hand side a $1:99$ diluted CSNP suspension was used to prepare the HM3 sample spot.

substrate was cleaned and $3\mu l$ drops were deposited onto it but with the help of a bigger $40\mu l$ capacity pipette. The same drop casting - drying cycle was performed several times until a homogenous solid distribution formed. This is visualized on the right hand side of Figure 4.4.

It was found that - as reported in reference [57] - the samples prepared with the undiluted and pure CSNP suspension was very susceptible to vibrations and small mechanical stress which resulted in cracks and detachment from the silicon wafer while transferring the Si wafer into the XPS equipment. While this was not the case for the diluted sample, depositing a large amount of drops onto the same spot to form a solid and thick enough layer of nanoparticles increases the preparation time significantly as the substrate needed to be dried after each drop cast.

Another challenge in the preparation of these insulating core-shell nanoparticle samples is the mentioned charging during the XPS measurements. On one hand the layer of the PTFE@PMMA nanoparticles on top of the Si wafer has to be thick enough to be able to measure a good signal with little to no contributions from the substrate. On the other hand the investigated particle layer has to be thin enough to minimize charging effects due to the insulating nature of the CSNP. Contrary to expectations from previous experiments, only for the sample prepared with the thick undiluted specimen charging in the mentioned XPS measurements at the TU Wien could be compensated with the previously stated electron flood gun settings. No explanation was found for this unexpected behaviour.

The measured XPS survey spectrum presented in Figure 4.5 was measured on the thick area of the prepared undiluted specimen (left image in Figure 4.4). Due to the thick

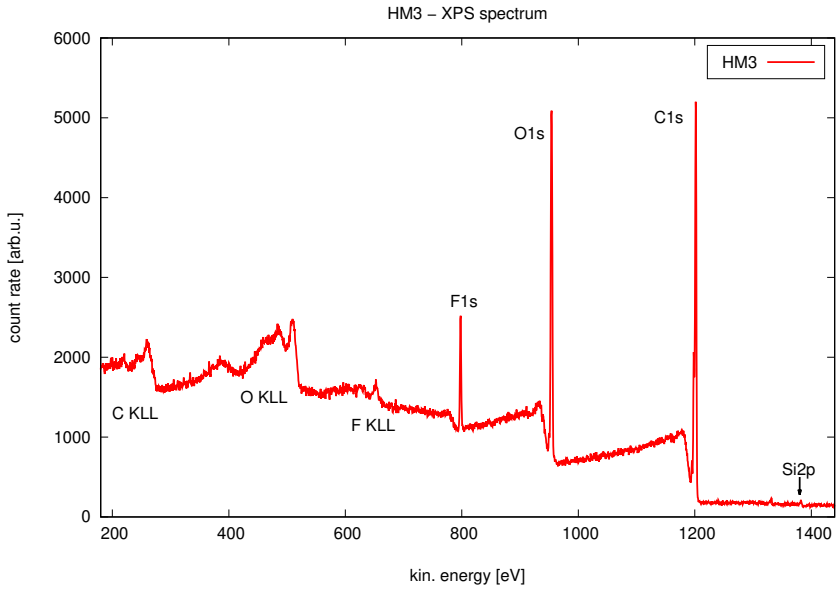

Figure 4.5: Survey XPS spectrum from HM3 PTFE@PMMA core-shell undiluted particle suspension taken at TU Wien.

particle film the characteristic silicon $Si2p$ peak representing the substrate is barely visible in the survey spectrum. Additionally to the respective elemental $1s$ XPS peaks present in the PTFE@PMMA particles, corresponding KLL Auger peaks were observed.

In the detailed XPS spectrum for the $C1s$ peak, Figure 4.6, a five component fit could reproduce the measured signal well. The four components C1-C4 were expected contributions of PMMA as mentioned in section 4.1. PTFE as the nanoparticles core material is represented as the fifth C5 component which - although relatively weak - is well separated from the other signal contributions.

Figure 4.7 shows the detailed XPS spectrum of the $O1s$ peak of the measured undiluted specimen measured in the described TU Wien XPS setup. As described in the previous section 4.1 the shell PMMA material is composed of two chemically shifted components $O1$ and $O2$. To fit the measured detailed $O1s$ XPS spectrum additionally to the two PMMA components a third $O3$ component needed to be added to reproduce the experimental peak data. This third $O3$ component was attributed to absorbed residual water at a binding energy of $536.7eV$.

For the detailed $F1s$ spectrum representing the nanoparticles core material PTFE a single component was enough to reproduce the measured XPS data shown in Figure 4.8.

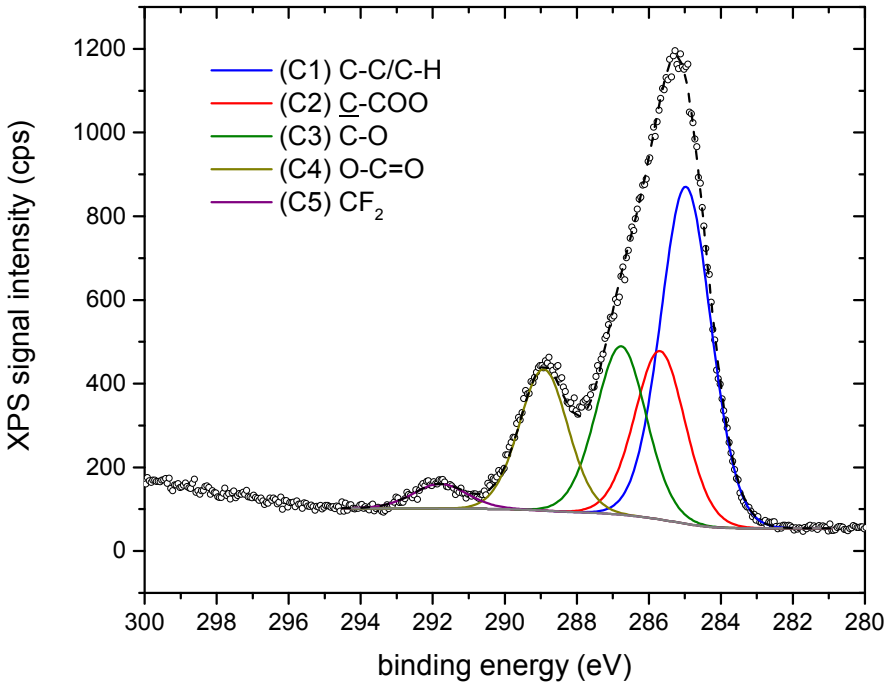

Figure 4.6: Detailed XPS spectrum of $C1s$ peak for the measured undiluted specimen at the TU Wien. C1-C4 representing chemically shifted components of PMMA, C5 representing the chemically shifted PTFE fraction of the $C1s$ peak.

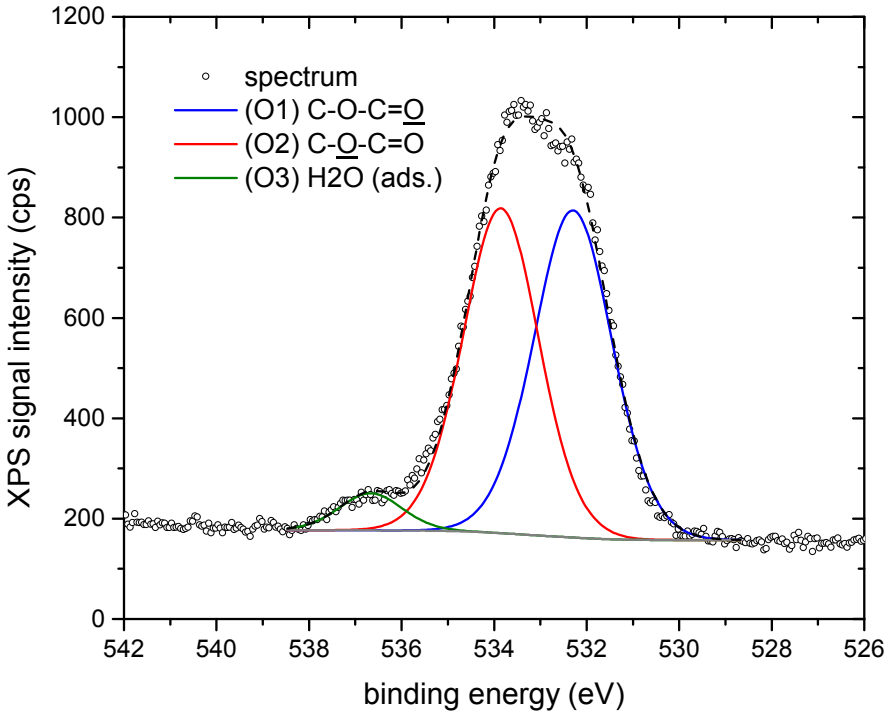

Figure 4.7: Detailed XPS spectrum of $O1s$ peak for the measured undiluted specimen at the TU Wien. $O1$ and $O2$ representing PMMA with an additional O3 contribution due to absorbed residual water.

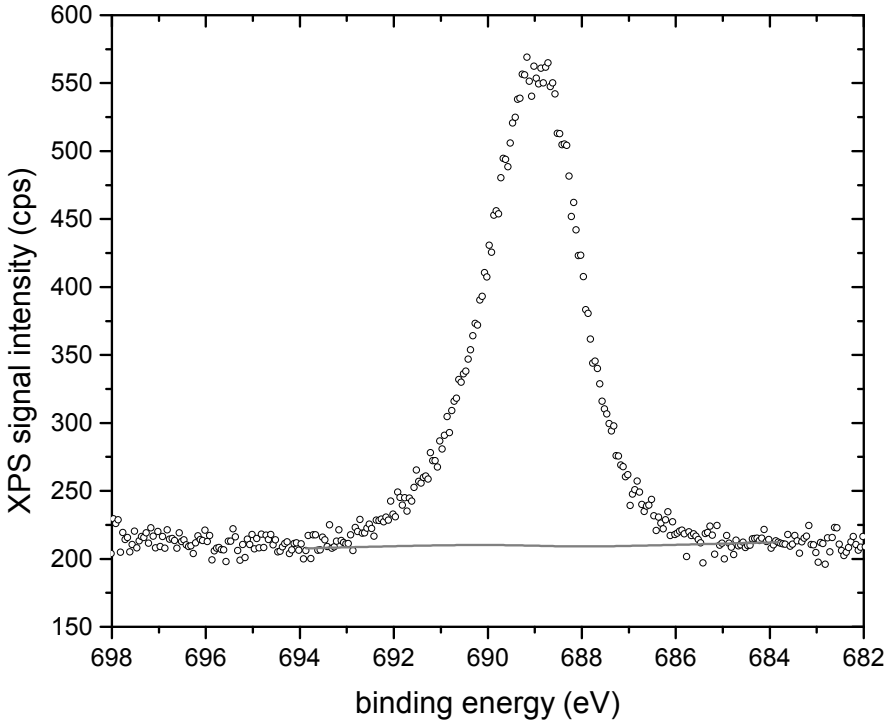

Figure 4.8: Detailed XPS spectrum of $F1s$ peak for the measured undiluted specimen at the TU Wien. A single component peak with good agreement in energy for organic fluorine.

Although when fitted the peak shape presents a slight asymmetry which might indicate a residual uncompensated sample charging.

To estimate shell thicknesses for the investigated core-shell nanoparticle, the measured XPS signals need to be further processed. Discussed methods for quantification in section 3.2 estimate these shell thicknesses based on peak intensity ratios. As described in section 4.1 the investigated HM3 core-shell nanoparticle consists of PTFE cores with a PMMA shell. Characteristic contributions to the XPS spectrum originating from the core (PTFE) can be either the $F1s$ XPS peak (Figure 4.8) or the $C5$ component of the $C1s$ signal (Figure 4.6). PMMA as the shell material on the other hand can be characterized by the $C1s$ peak components $C1 - C4$ (Figure 4.6) or by the $O1s$ XPS signal (Figure 4.7).

This results in four different shell to core ratios represented in the first panel of Table 4.1 calculated for each institutes XPS data set. The reported XPS data sets were corrected by the corresponding instruments transmission function. Since the used quantification methods utilize the straight line approximation and thus neglect energy dependencies for scattering events further corrections such as the relative sensitivity factors were not applied.

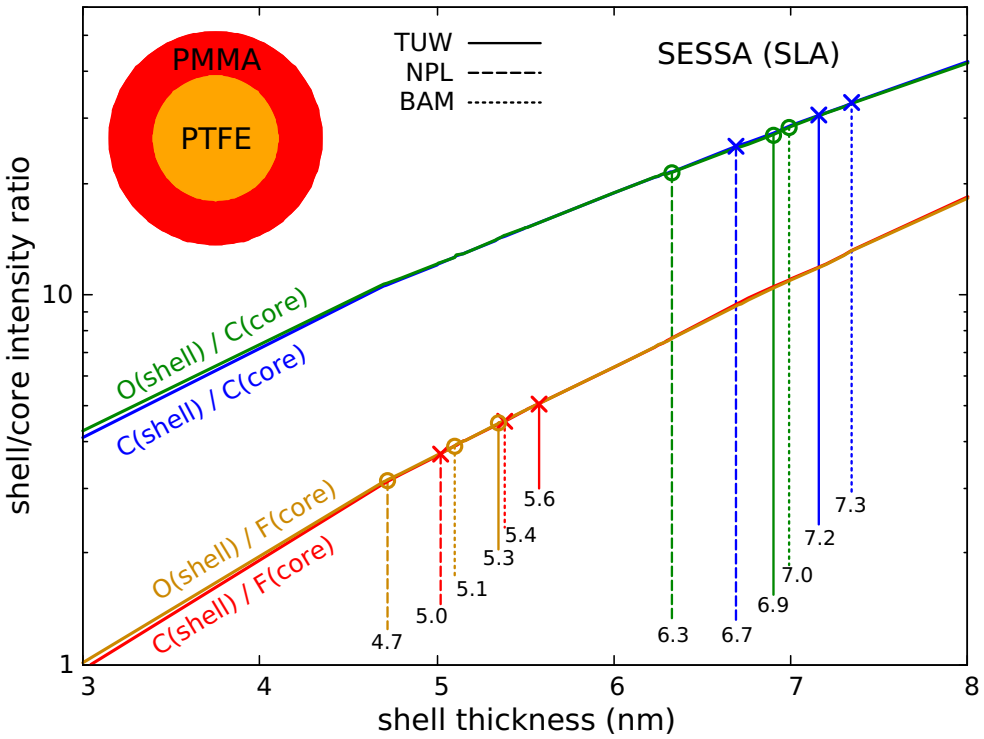

Figure 4.9: Calibration curves (solid lines) calculated by SESSA with applied straight line approximation for CSNP using a PTFE core and a PMMA shell material. Experimental XPS peak intensity ratios are noted by corresponding institutes. Circles indicate ratios representing the PMMA shell via the oxygen signal. Crosses indicate ratios representing the shell material PMMA via the carbon signal. The different colours indicate the the different datasets of core-shell ratios.

As SESSA has the ability to simulate spectra according to a given experimental setup, calibration curves for the shell thickness estimation were calculated for each participating institute (BAM, NPL, TUW). Since the source-sample-analyser angle for the participating institutes' XPS setups are very similar, one calibration curve per ratio could be used.

Generally the calibration curves, visualized in Figure 4.9, for different shell to core ratios are not expected to coincide. However due to the combination of the necessary parameters for the simulation the different signals of $C1s$ and $O1s$ did not impact the resulting ratios representing the shell PMMA material. Therefore the graph shows four solid calibration lines in pairs of two, differing only in the representation used for the PTFE core signal ($C(core)$ or $F(core)$).

The partner institutes findings for the measured XPS peak intensities reported in Table 4.1

are referenced in Figure 4.9 - resulting in very promising shell thickness estimations around the expected value of $7nm$ for ratios based on the cores carbon contributions from the PTFE material.

The second panel in Table 4.1 reports estimated shell thicknesses based on calculated SESSA-SLA calibration curves for the reported XPS data from inter-laboratory round-robin study. The third panel is based on IC model calculations for the reported shell to core ratios. The last panel represents estimated shell thicknesses based on the T_{NP} formula described in subsection 3.2.1.

Interestingly, all thickness estimations - which are based on the core-shell nanoparticles core being represented by the carbon contribution from the PTFE material - are close to the expected $7nm$, taking into account the models expected uncertainties of around 10%. These findings are very satisfying since the measurements were done in different X-ray photoelectron spectroscopes, prepared under different conditions by each partner institute.

However, thickness estimations based on the core being represented by the $F1s$ XPS signal intensities were deviating significantly from the expected $7nm$ shell thickness. This again is consistent for all applied quantification methods and every XPS data set taken by the inter-lab study participants. Layers of adventitious contamination might explain parts of these deviations, as additional inelastic scattering would occur and thus the signal would be further attenuated. Yet the detailed XPS spectra only suggest small contamination levels therefore these deviations could not solely be due to sample impurities.

A more likely explanation for these significant deviations in the shell thickness estimations based on the $F1s$ signals are structural or compositional defects such as diffusion of fluorine into the PMMA shell.

The simulation of mentioned calibration curves in combination to the mentioned inter-lababoratory study were reported in the Innanopart projects activity report A3.3.3. For further details on the XPS measurements done in this study refer to the Innanopart projects deliverable D6, which extensively discussed the XPS data, sample preparation in each laboratory and shell thickness determination and interpretation.

4.3 XPS spectra simulations of core-shell nanoparticles

Since the electron beam techniques showed that the investigated CSNP have mostly non ideal geometric character and due to the inconsistencies in the XPS data interpretation, SESSA simulations were performed to investigate the impact of observed features on the XPS signals and consequently the impact these features might have on the shell thickness determination. PENGEOM geometries describing a single porous core-shell nanoparticle and powders consisting of these CSNP structures were created and simulated. Powders with pores and acentric cores were created since these structures compare to a high

Table 4.1: Detailed comparison of results obtained by the inter-lab study. The intensity ratios in the first table represent the experimental data obtained by the XPS measurements, corrected with the corresponding instruments transmission function. The second table shows a comparison of estimated shell thicknesses based on calibration curves calculated via SESSA using the straight-line approximation method and the measured experimental XPS data. The third table represents the same analysis but based on the IC model. The last table represents the estimated shell thicknesses based on the T_{NP} formula calculated from the inter-lab studies' partners measured XPS data.

experimental data	intensity ratios		
line pair	BAM	NPL	TU Wien
C 1s (PMMA) / C 1s (PTFE)	32.90	25.15	30.58
C 1s (PMMA) / F 1s (PTFE)	4.53	3.70	5.08
O 1s (PMMA) / C 1s (PTFE)	28.34	21.39	27.01
O 1s (PMMA) / F 1s (PTFE)	3.90	3.15	4.48

SESSA (SLA)	estimated shell thicknesses (nm)		
line pair	BAM	NPL	TU Wien
C 1s (PMMA) / C 1s (PTFE)	7.34	6.69	7.16
C 1s (PMMA) / F 1s (PTFE)	5.38	5.02	5.58
O 1s (PMMA) / C 1s (PTFE)	6.99	6.33	6.90
O 1s (PMMA) / F 1s (PTFE)	5.10	4.72	5.35

IC model	estimated shell thicknesses (nm)		
line pair	BAM	NPL	TU Wien
C 1s (PMMA) / C 1s (PTFE)	7.38	6.72	7.20
C 1s (PMMA) / F 1s (PTFE)	5.42	5.06	5.63
O 1s (PMMA) / C 1s (PTFE)	7.01	6.32	6.90
O 1s (PMMA) / F 1s (PTFE)	5.14	4.76	5.39

T_{NP} **formula**	estimated shell thicknesses (nm)		
line pair	BAM	NPL	TU Wien
C 1s (PMMA) / C 1s (PTFE)	7.23	6.65	7.10
C 1s (PMMA) / F 1s (PTFE)	5.30	4.97	5.50
O 1s (PMMA) / C 1s (PTFE)	6.97	6.38	6.91
O 1s (PMMA) / F 1s (PTFE)	5.09	4.76	5.36

degree to the real world observations - visibly in the STEM images of the previous chapters: Figure 4.12, Figure 4.13 and Figure 4.14.

Figure 4.10 and Figure 4.11 show the data analysis of the shell to core peak ratios for distinct modelled features and to which degree it impacts these ratios.

The graphs shows calculated ratios for single ideal core-shell nanoparticles: “Sphere” - which represents the SESSA internal geometry - and “Sphere-geo”, which represents a generated PENGEOM geometry which is loaded into the simulation. This was done to validate the later procedure.

Next morphologies simulated were porous core-shell nanoparticles represented by “Single Pore” followed by an angle. These were simulate to compare the impact a pore in a single core-shell nanoparticle has on the shell to core signal ratio with different orientation towards the XPS detector.

As a representation of core-shell nanoparticle agglomerations a powder of ideally shaped core-shell spheres is used, denoted by “Powder” in the graphs. To be able to compare the impact distinct features have on the shell to core ratios, a powder geometry based on core-shell nanoparticles with acentric cores is represented by “Powder Acentric 80%” in the graph. The “Powder Pore” simulation is a powder geometry based on porous core-shell nanoparticles morphologies. The ratio denoted by “Powder Pore Acentric 80%” features a simulation of a powder formed by porous core-shell nanoparticles with acentric cores, exhibiting a combination of observed features.

SESSA version 2.1 was used for calculating the simulated spectra, giving the ability to utilize the PENGEOM sample geometries with interpretations of the observed features. As mentioned in section 4.1 the HM3 particles have an average core diameter of $47nm$ and a estimated shell thickness of $7nm$.

The pores which are represented as circular openings in the shell of the nanoparticle morphology were set to a fixed diameter of 20% of the particle size.

For the powder calculations with acentric cores, the core offsets were distributed normally with a factor of 80% standard deviation of the shell thickness. For further details refer to the SESSA manual [40] section 8.3.1 were the PENGEOM geometry generator program for disperse powders is documented.

The geometrical conditions for the simulations were set emphasising fast simulation times, thus the samples normal axis was set in the same direction as the analyser axis $\phi = \theta = 0°$. An $AlK\alpha$ source was defined with an axis configuration of $\phi = 0°, \theta = 60°$ to the sample surface normal. As for the analyser, its aperture opening angle was configured to $\theta = 0 - 15°$. Additionally the simulations convergence value of $3e^{-}6$ was set and only XPS peaks necessary for the comparison were calculated.

For the shell material PMMA a mass density of $1.18g/cm^3$ and an energy gap of $6.7eV$ was used. The shell signal peaks simulated were $O1s$ with $E_{kin} = 943.5eV$ and the

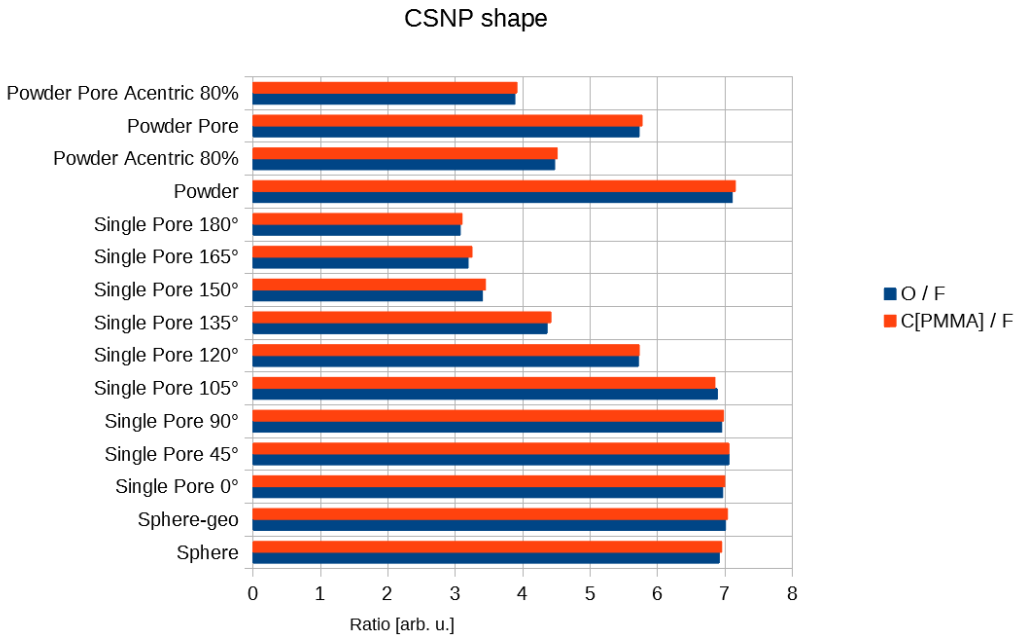

Figure 4.10: Core/Shell peak intensity ratios for PTFE@PMMA particles with the F signal representing the core. Ratios are calculated for distinct features identified by electron microscopy methods.

corresponding chemically shifted PMMA carbon $C1s$ peak represented as $C[PMMA]$ at the position of $E_{kin} = 1201.7eV$.

PTFE as the core material was simulated with a mass density of $2.17g/cm^3$ and an energy gap of $7.2eV$. Simulated peaks representing the core were the $F1s$ with a kinetic energy of $E_{kin} = 789.9eV$ and the chemically shifted PTFE carbon $C1s$ peak represented as $C[PTFE]$ at the kinetic energy of $E_{kin} = 1194.7eV$.

The simulations represented in Figure 4.10 and Figure 4.11 show that for powders - consisting of geometrically ideally shaped core-shell nanoparticles - and single spheres the core-shell peak rations are very similar, which is expected and supported by reference [58]. This powder approximation is often used for simplification of simulations, but is only valid for peak ratios as the XPS background signals might differ significantly. Although the scales of Figure 4.10 and Figure 4.11 are different for different representations of the core signal - F or $C[PTFE]$, the behaviour of the core-shell peak ratios have no strong dependency on the shell signal representation used for calculation of the ratios - O or $C[PMMA]$.

Furthermore one can see a strong dependence on pores and their orientation for single CSNP. This is understandable due to the surface sensitivity of the measuring method. The XPS detector receives higher intensities of the core signal, since the simulations

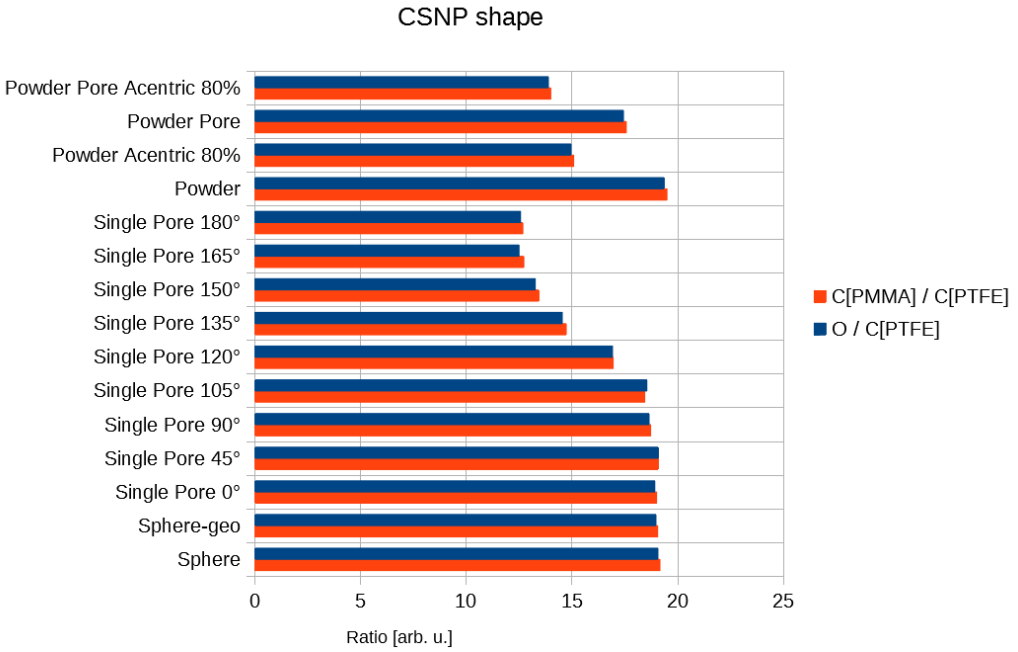

Figure 4.11: Core/Shell peak intensity ratios for PTFE@PMMA particles with the $C[PTFE]$ chemically shifted signal representing the core. Ratios are calculated for distinct features identified by electron microscopy methods.

with higher angles ($120° - 180°$) exposes the core directly to the detector.

Powders consisting of single CSNP with pores show a smaller than expected impact in the core-shell ratio. This might be explained due to the random orientation of the CSNP the powder consists of and consequently the single CSNP pores' orientation. The pores opening will be randomly oriented over all possible angles and therefore the ratios are only slightly changed.

A much bigger impact on the core-shell ratios show powders consisting of acentric CSNPs in contrast to a powder consisting solely of ideally shaped core-shell nanoparticles. As visible in the STEM images, the majority of CSNP have an asymmetric character and therefore this feature can have a big impact on the shell thickness determination methods. Which base assumption is, that the core-shell nanoparticles are ideally spherically shaped. The additional impact pores have on the signal ratio of powders with acentric cores is minimal in contrast to the impact asymmetric cores have on the signal ratio.

4.4 Electron beam analysis

As discussed in section 4.2 in the small inter-laboratory XPS study with other institutes it could be shown that the calculated shell thicknesses depended on the used core peak signal which lead to different explanations. For a better understanding of the investigated CSNP additional electron beam techniques (TEM, TEELS and EDX) were used to get a visual representation of a typical nanoparticle from the HM3 suspension.

4.4.1 Scanning transmission electron microscopy

The Sample preparation was done via drop-casting the CSNP sample solvent onto a carbon support film which was dried in the pre-vacuum when inserted into the microscopes load lock. All of the performed electron beam analysis techniques were done with an *FEI Tecnai F20*[4] microscope. The acceleration voltage was set to $200kV$ with a beam current of $0.358nA$. For the scanning transmission electron microscopy (STEM) images both annular bright-field (ABF) and high-angle annular dark filed (HAADF) modes were employed, see Figure 4.12. Due to the higher atomic number sensitivity of the HAADF mode, images recorded in this mode have better contrast. These recorded images were further optimized for contrast.

As already can be observed in Figure 4.12 the specimens core-shell structure is visible but has a strong asymmetric character. Overall the CSNP in the investigated HM3 sample drops were mostly acentric core-shell geometries and thus had strongly varying local shell thicknesses.

In the top images which are taken in ABF mode the cores are darker with a lighter shell wrapped around it. The top left image shows that four particles are cobbled together making it difficult to determine exact dimensions, although all particles seem to be within the estimated dimension of $\sim 50nm$. Rough visual shell thickness estimations were done with the top right image were a single particle with better defined core borders is represented.

The two bottom images are taken in HAADF mode, representing the heavier elements of the PTFE core brighter than the lighter PMMA shell materials. The bottom left image in Figure 4.12 again shows bonding core-shell nanoparticles making it difficult for visual shell thickness determination, although it can be confirmed that the core-shell structure of the particles and the overall dimension are in the estimated range. As in the top right image visual shell thickness estimations were done on the bottom right image, due to the better contrast it is easier to determine the transition between core and shell.

Overall the STEM images showed that the dimension of the CSNP are in the predicted $56nm$ size but with strongly irregular shell thicknesses ranging from $3nm$ to $17nm$. Although visual determination of the shell thicknesses is difficult due to the

[4] https://www.ustem.tuwien.ac.at/instrumentation/fei_tecnai_f20/EN/

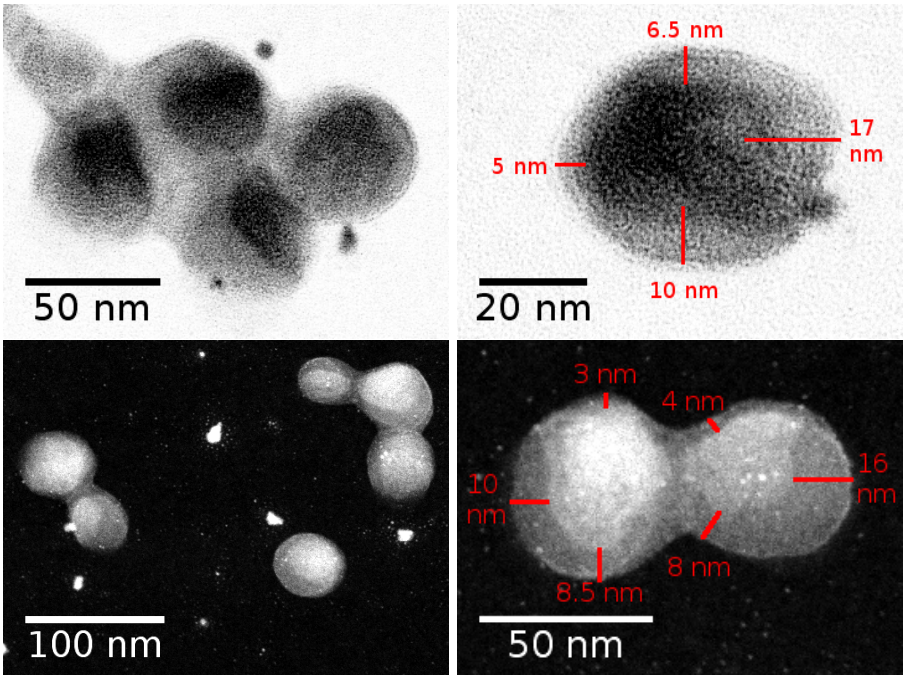

Figure 4.12: STEM images (optimized contrast) of the investigated HM3 CSNP, top taken in ABF mode and bottom in HAADF mode.

vague core-shell transitions a rough shell thickness determination of single nanoparticles was possible.

Additional small features are visible in the images usually around 5 to 15nm in size. Elemental analysis of these shapes showed them to be sulphurous depositions probably in the carbon layer of the used support grid. Presumably residues from the manufacturing process of those support films. As a test, new and clean support films were used showing similar abnormalities. No interaction between those residues and the investigated CSNP were observed.

4.4.2 Energy dispersive X-ray spectroscopy in the STEM

As mentioned in the previous section, the energy dispersive X-ray (EDX) line scans were taken in the same microscope as the STEM images. Attached to the electron microscope is a *AMETEK Apollo XII* detector for X-ray detection. For details on the EDX process refer to subsection 2.2.2.

The EDX line scans taken produce higher radiation damage because of a relatively long acquisition time of about a second per position with a step distance of 1.5nm along a trace. The scanned trace is represented in the top ABF-STEM image of Figure 4.13. This radiation damage is visible in the HAADF-STEM image in the top of Figure 4.14

which was taken after the EDX line scan and before the TEELS line scan on the same core-shell nanoparticle.

The middle graph in Figure 4.13 shows the taken EDX line scans, again revealing the core-shell structure of the investigated HM3 nanoparticles. These EDX line scans were obtained by integration over a fixed energy range around a peaks maximum. The graph shows the fluorine $K\alpha$ signal in the centre of the scan surrounded with a wider oxygen $K\alpha$ signal as a shell around it. Although difficult to measure accurately - in particular since the EDX line scan taken is not centred inside the particle and the STEM images showing how asymmetric the CSNP is - the particles local core dimension taken along the trace can be estimated to be in the dimension range of about $38nm$. With the Help of the oxygen $K\alpha$ signal representing the shell, even the shell thickness could be estimated from this EDX line scan to be around $6nm$. Although that with this technique the shell thickness and the core diameter could be estimated to be in the expected range, this EDX line scan had a limited spatial resolution and can measure only one single particle at a time. This and the limit in measurement time due to the radiation damage are drawbacks of this experimental technique.

In addition to the EDX line scan two EDX spectra along the scanned trace were taken at the marked positions - dashed vertical bars. The two detailed EDX spectra taken are represented in the bottom graph of Figure 4.13, one spectrum was taken in the CSNP centre and a second one in a shell position of the sample. These detailed scans show that the fluorine $K\alpha$ signal is only present in the spectrum taken in the centre position.

As carbon (C) is present in both PMMA and PTFE the EDX spectra show for both position contributing $K\alpha$ signals, an additional distinction of origin of the carbon signal is not possible. However the carbon signal in the shell position is much smaller than in the centre position of the particle which indicates a higher relative oxygen concentration for the shell, which is consistent for the expected core-shell morphology.

Since the particle is presumably wrapped with a PMMA shell both detailed EDX spectra exhibit signs of detected oxygen $K\alpha$ X-rays, as these have a much bigger penetration length in the μm excited X-rays can pass through the sample and thus be detected. Additionally the broad oxygen and fluorine $K\alpha$ signals represented in the bottom graph of Figure 4.13 with energy width in the order of $100eV$ might be falsely contributing to the intensity of the two EDX line scan signals, resulting in a very similar $OK\alpha$ signal across the entire CSNP. Which would further decrease the lateral resolution of the line scan.

A small signal contribution of the supporting copper (Cu) grid is also present in both EDX spectra.

4.4.3 Transmission electron energy loss spectroscopy

The transmission electron energy loss spectroscopy (TEELS) line scan was taken in the same scanning transmission electron microscope at same conditions and on the same

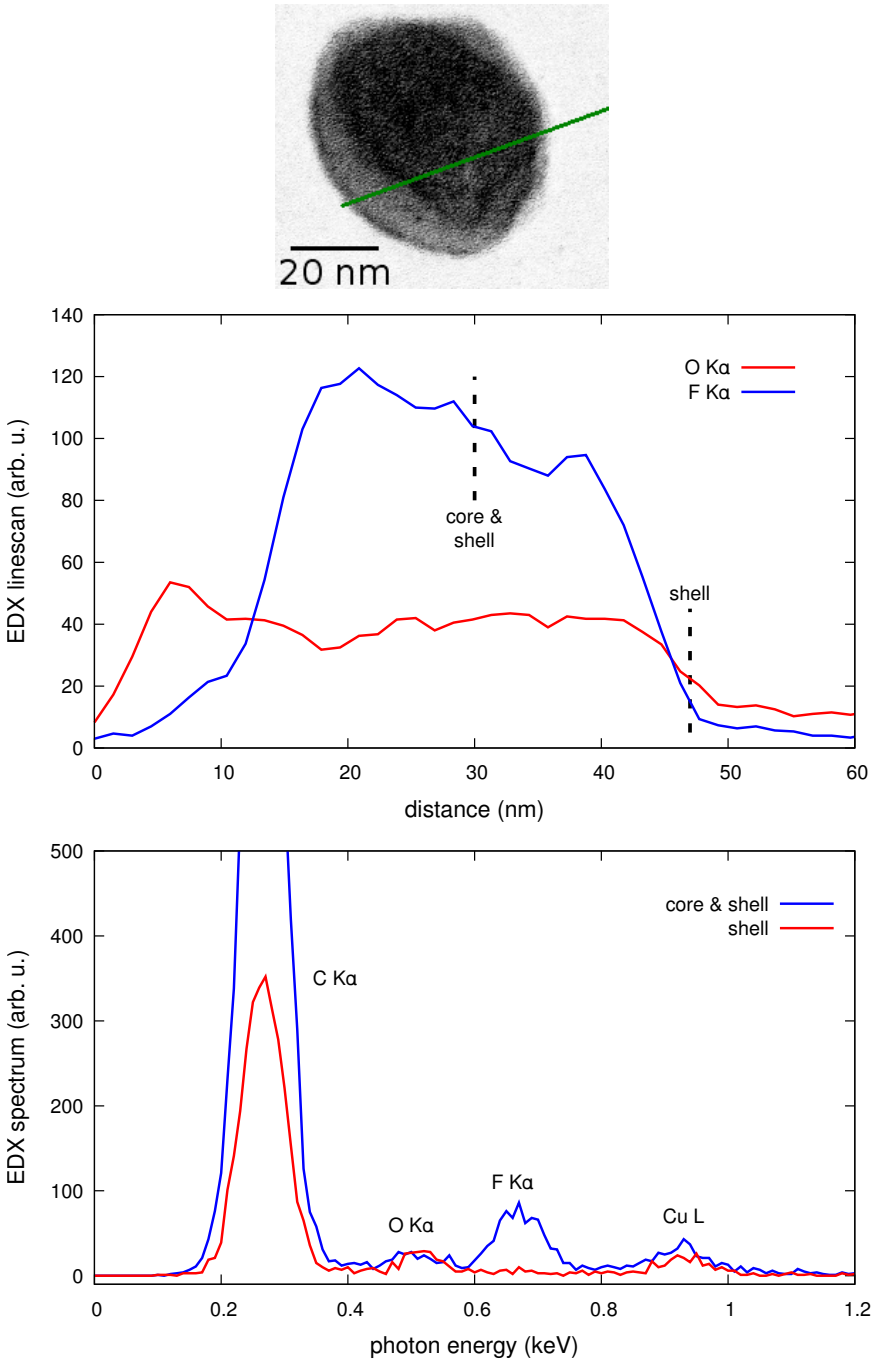

Figure 4.13: ABF-STEM image (top, optimized contrast) green line showing where the EDX line scan (middle, smoothed by moving average) was taken. The EDX spectra (bottom) were taken along the line scan trace at locations indicated by the dashed vertical bars.

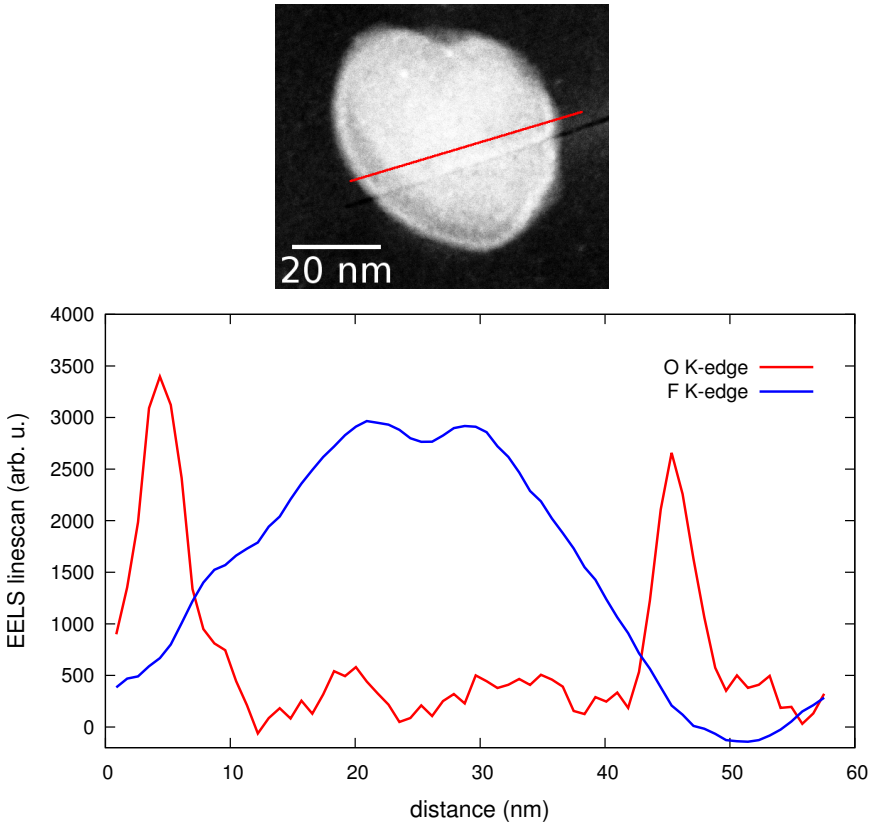

Figure 4.14: HAADF-STEM image (top, optimized contrast) the red line is showing the trace taken for the TEELS line scan (bottom). Below the red line in the STEM image an additional trace is visible due to beam damage of the previously taken EDX line scan. The TEELS line scan reproduces the core-shell structure of the nanoparticle with dimensions in the expected range. Due to the weak signal the oxygen K-edge intensity was scaled by a factor of 20.

core-shell nanoparticle as the previous EDX line scan. For signal collection a *Gatan GIF Tridiem* spectrometer is attached to the spectroscope. For details on the TEELS process refer to subsection 2.2.3.

The top HAADF-STEM image of Figure 4.14 shows the path taken for the TEELS scan, to avoid the damage produced by the previously taken EDX line scan a slightly different trace for the TEELS line scan was taken. As in the previous HAADF-STEM images the core is represented lighter and the shell is darker. As both the TEELS line scan and the EDX line scan were taken from the same CSNP the HAADF-STEM image and the ABF-STEM image in the top of Figure 4.13 show how asymmetric this CSNP is and how thin the shell thickness on one side is. Nevertheless the dimension of the CSNP fits the estimated prediction.

The bottom TEELS line scan of Figure 4.14 verifies the CSNP dimension to be within the reference range of about $50nm$. With a core size of about $35nm$ and local shell thicknesses of about $5nm$, these findings confirm the EDX findings. In addition to the EDX line scan the TEELS line scan confirms the core-shell structure of the particle, visible due to the oxygen peaks describing the shell and the centre fluorine signal as a representation for the core.

4.5 Comparison of models for inelastic scattering

In chapter 3 the default quasi-elastic model and the newly implemented true slowing down model were described, and possible improvements to the default simulations model of SESSA were considered.

The default simulation model of SESSA uses the quasi-elastic approximation (QEA) which assumes that the energy loss occurring in inelastic scattering events is small compared to the primary energy of a projectile electron and thus the energy dependence of the scattering parameters (mean free paths and cross sections) can be neglected.

This is in big contrast to the computation intensive true slowing down (SDN) method were at each collision event the energy losses are fully taken into account and according adjustments to the IMFP and the cross sections are taken into account producing a physically more realistic simulation.

As an alternative to the computation intensive SDN method the enhanced QEA+ method, which is post processing the simulated QEA-XPS spectrum with a normalization factor taking into account the overall IMFP behaviour, is shown for comparison. For the QEA* method a more elaborate post processing is done compared to the QEA+ method - here the overall IMFP behaviour was not only applied to the finished full QEA-XPS spectrum but on each single peak spectrum which make up the final full XPS spectrum.

Simulations were setup to optimize the simulation time of the SDN calculations the aperture opening angles were set to $\phi = 0 - 360°, \theta = 0 - 90°$. The axis orientations of the sample surface normal and the source axis were set to $\phi = 0°, \theta = 0°$. The orientation of the analyser axis was set to $\phi = 0°, \theta = 60°$. The default energy source $AlK\alpha$ was kept with the characteristic kinetic energy of $E_{source} = 1486.6eV$. The simulations were done for the default spectrometer range of a lower kinetic energy boundary of $E_{kin} = 600$ till the upper limit of $E_{kin} = 1500eV$. Furthermore the number of simulated trajectories for the SDN method were set to 10 million.

In Figure 4.15 a simple geometrical situation was chosen to compare the different simulation methods. An aluminium infinite plane sample was defined with only one single peak $Al2p_{3/2}$ at the kinetic energy of $E_{kin} = 1414eV$, it was calculated to compare the different simulation models. For comparison, the simulated QEA and SDN XPS spectra were normalized to the $Al2p_{3/2}$ peak height.

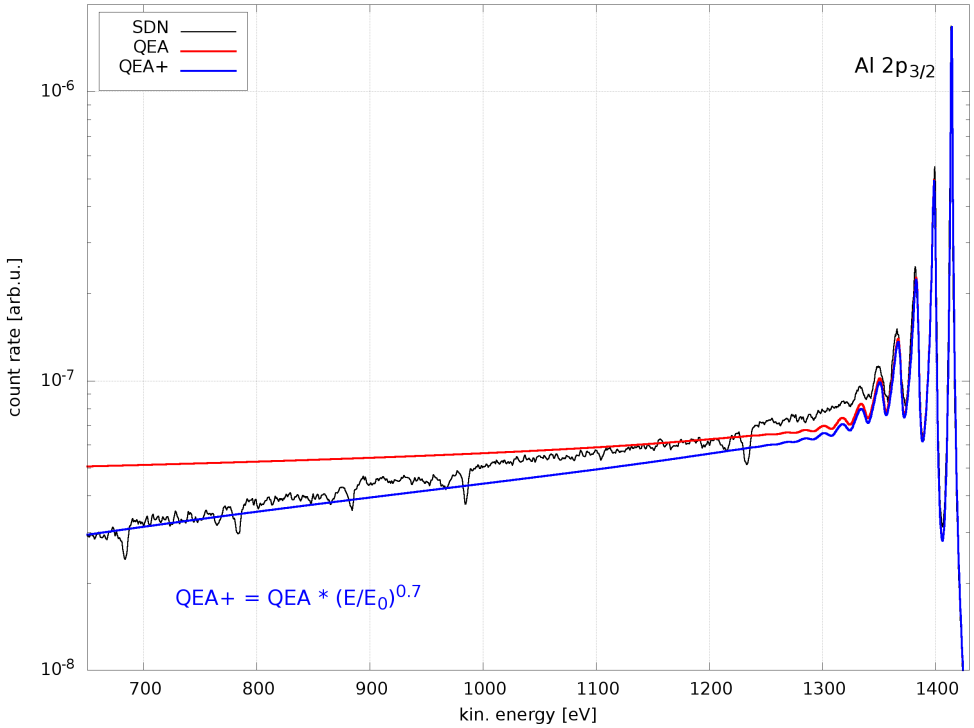

Figure 4.15: Simple geometry simulation with single peak XPS spectrum for model comparison, normalized to $Al2p_{3/2}$ peak height for comparison.

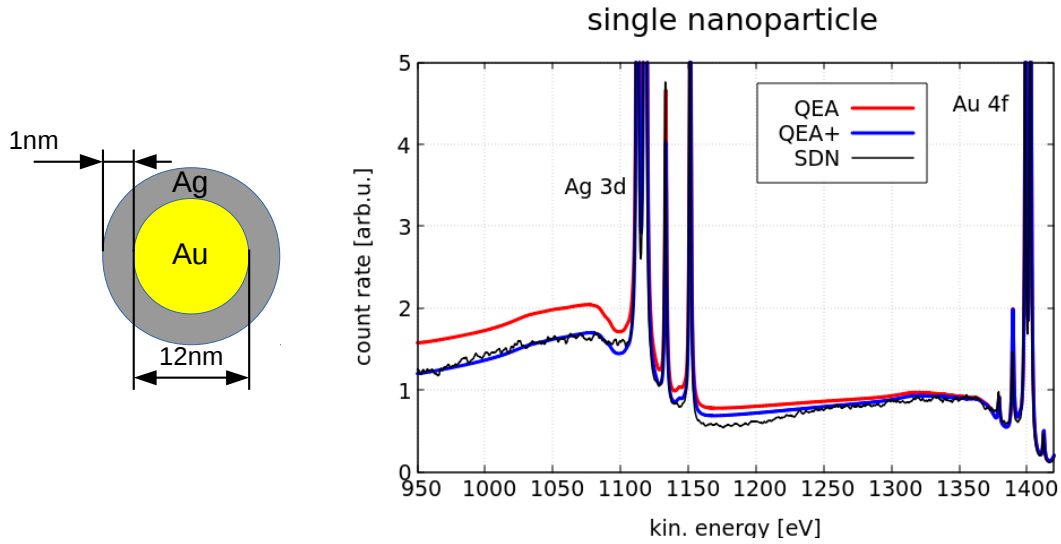

Figure 4.16: Single Ag@Au CSNP XPS spectra for comparing different simulation models of a complex geometry. For comparison the data are normalized to the $Au4f$ peak.

Figure 4.15 shows by comparison between the QEA and the newly implemented SDN simulation method, that the SDN method clearly reproduces the plasmons in the kinetic energy range of $\sim 1300-1400eV$ followed by the elastic $Al2p_{3/2}$ peak at $E_{kin} = 1414eV$. Although there is some noise visible in the SDN data, the method is able to reproduce the overall spectrum and distinct features of this spectrum.

To validate the hypothesis documented in subsection 3.1.3 were the overall IMFP behaviour is added to the QEA simulation by normalizing the QEA spectrum, Figure 4.15 represents QEA+ as this extension of the QEA model. The crude QEA+ method is able to reproduce the overall behaviour of the SDN method very closely. Since the QEA+ is able to utilize the trajectory reversal method (TRM) the simulation times are much lower compared to the SDN method, because only a fraction of trajectories needs to be simulated.

The next step was to verify and compare the models with a more complex sample morphology. Simulations were performed for a single core-shell nanoparticle with a $1nm$ thick silver (Ag) shell and a $12nm$ in diameter gold (Au) core, represented on the left hand side of Figure 4.16.

Source type, spectrometer geometry and further simulation conditions were set to the same conditions and values as previously described. On the right hand side of Figure 4.16 the resulting XPS spectra for model comparison are represented, the figure shows that even for a complex sample morphology such as a core-shell nanoparticle composed of different elements the SDN method and the QEA+ method are in a good agreement.

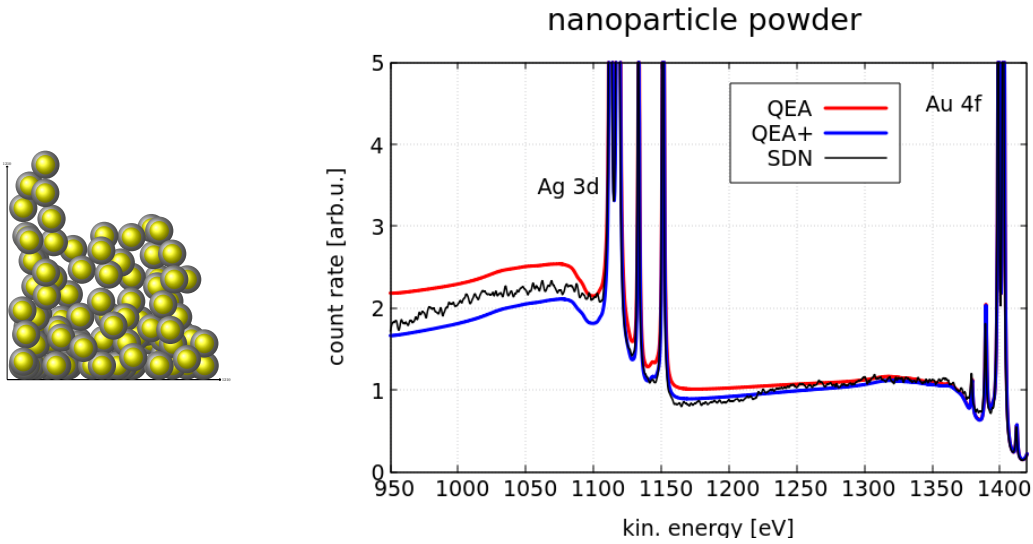

Figure 4.17: XPS spectra for different simulation models of a powder consisting of AG@Au CSNP. For comparison reasons the data is normalized to the $Au4f$ peak.

Here the main focus lies on the very good agreement of the XPS signal background for these two different simulation models. For comparison the simulated XPS spectra were normalized to the $Au4f$ peak, which was also the peak the QEA+ approach was calculated from.

To compare the models for realistic sample morphologies a powder of previously described $Ag@Au$ core-shell nanoparticles was created, represented on the left hand side of Figure 4.17. The simulation conditions from the previous simulation were used to have a common basis for comparison. On the right hand side of Figure 4.17 the resulting XPS spectra for the mentioned powder is shown. It was normalized to the $Au4f$ peak with the QEA+ calculation starting from that peak. The figure shows that the QEA+ model fails to replicate the simulation calculated via the SDN model, as the XPS background signal is composed of additional contributions due to the powder geometry.

To verify the proposed QEA* as an enhancement to the QEA+ method, simulations were performed including the including the compute intensive SDN model and SESSAs default QEA model.

Figure 4.18 represents XPS spectra simulated with the different methods of a simple pure gold (Au) substrate morphology. The simulated XPS peaks are represented in the first panel of Table 4.2. For comparison the simulated XPS spectra were normalized to the highest $Au4f_{7/2}$ peak for the SDN and the QEA methods. The QEA* can reproduce the SDN simulation very well although slight anomalies are visible around the peak $Au5s$ in the energy range between 1360-1390eV.

Table 4.2: Simulated XPS peaks and their corresponding kinetic energies in eV.

XPS peak	kin. energy
$Au4s$	724.5eV
$Au4p_{1/2}$	843.9eV
$Au4p_{3/2}$	940.3eV
$Au4d_{3/2}$	1133.4eV
$Au4d_{5/2}$	1151.5eV
$Au5s$	1379.4eV
$Au4f_{5/2}$	1399eV
$Au4f_{7/2}$	1402.7eV
$Au5p_{1/2}$	1412.4eV
$Au5p_{3/2}$	1429.4eV

XPS peak	kin. energy
$Cu3s$	1364.1eV
$Cu3p_{1/2}$	1404.3eV
$Cu3p_{3/2}$	1411.5eV

XPS peak	kin. energy
$Si2s$	1336.9eV
$Si2p_{1/2}$	1386.8eV
$Si2p_{3/2}$	1387.4eV

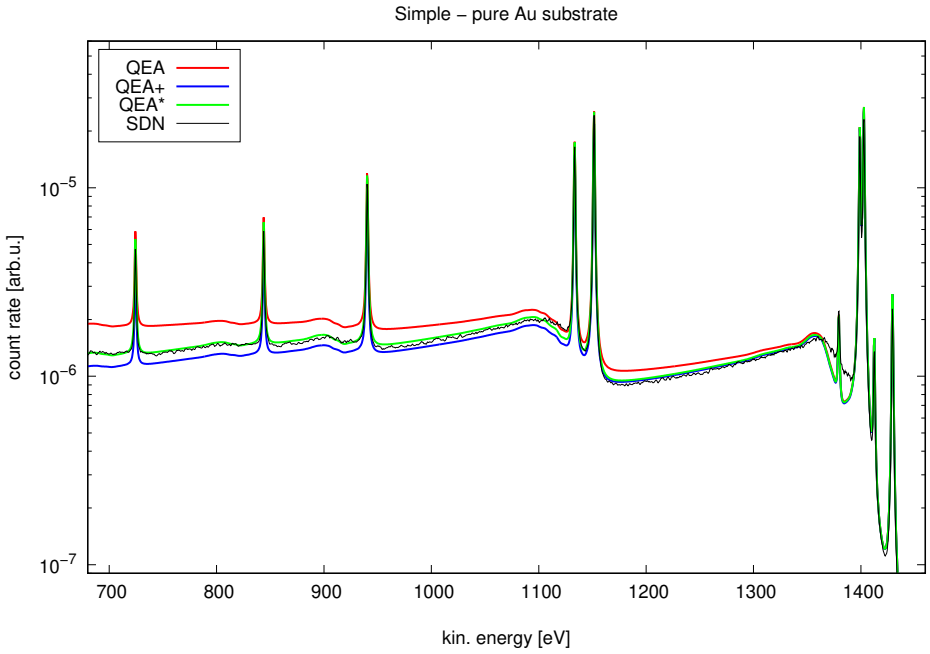

Figure 4.18: Comparison of different simulation methods for a simple pure Au substrate.

As suspected the peak intensities for the QEA* method are better reproduced than in the QEA+ method and the overall XPS background signal fits the SDN simulation very closely.

As a second step the previous gold (Au) substrate geometry was expanded by a planar copper (Cu) layer with a thickness of 5 Å. Figure 4.19 represents the simulated XPS spectra for the different simulations models with additional XPS peaks for the surface copper layer at kinetic energies represented in the second panel of Table 4.2. Due to the additional XPS peaks in the energy range above $1350eV$ the XPS background of the SDN simulation varies relatively to the QEA simulations. Nevertheless the overall full spectrum and the XPS peak intensities are still reproduced very well by the enhanced QEA* simulation method.

For an even more complicated sample morphology a core-shell nanoparticle with a gold (Au) core having a diameter of $12nm$ and a copper (Cu) shell with a thickness of 5 Å on a silicon (Si) substrate were simulated. Additional to the previous XPS peaks Figure 4.20 shows also the silicon substrate XPS peaks at kinetic energies represented in the last panel of Table 4.2. While the overall trend of the XPS full spectrum is correlated between the SDN and the QEA* method, the amount of different XPS peaks in the energy range

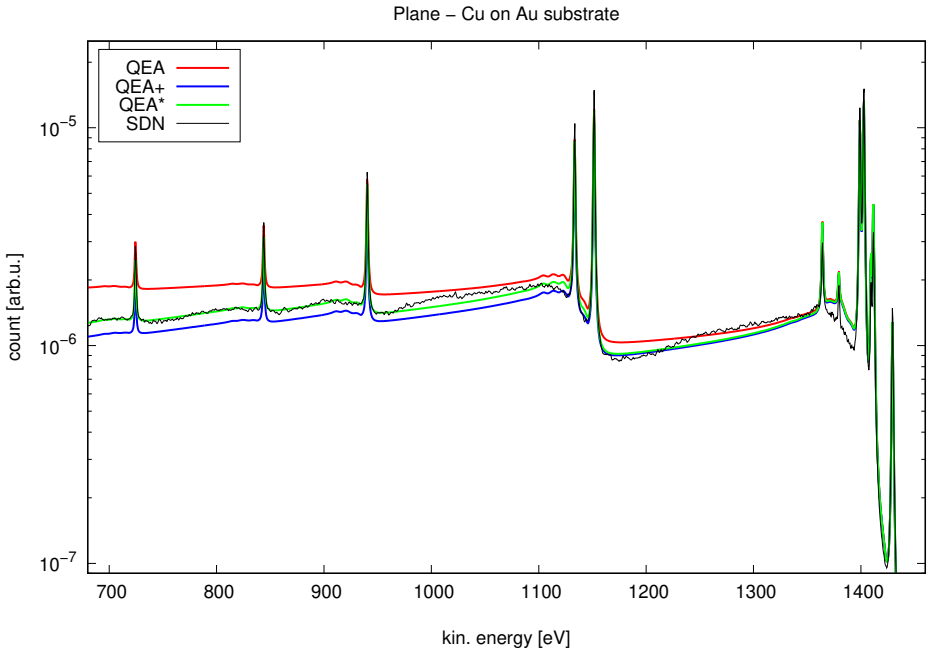

Figure 4.19: Comparison of different simulation methods for a Cu planar layer on Au substrate.

above $1350eV$ makes it difficult for the QEA* method to reproduce the XPS background accurately.

To summarize, the quasi-elastic approximation (QEA) can reproduce the XPS spectra created with the complex true slowing down (SDN) method within 10% of the primary electron energy quite well. For bigger electron energy losses the resulting XPS backgrounds reproduced by the QEA model show deviations to the physically more accurate - although computationally more intensive - true slowing down model, which is a disadvantage for quantitative analysis purposes. The proposed enhancements, QEA+ and QEA*, are post processing the simulated quasi-elastic XPS spectra by taking into account the overall energy dependency of the inelastic mean free path. These are conceptually easy and computationally cheap methods which reproduce the far more complex SDN XPS spectra very well in an easy and efficient way.

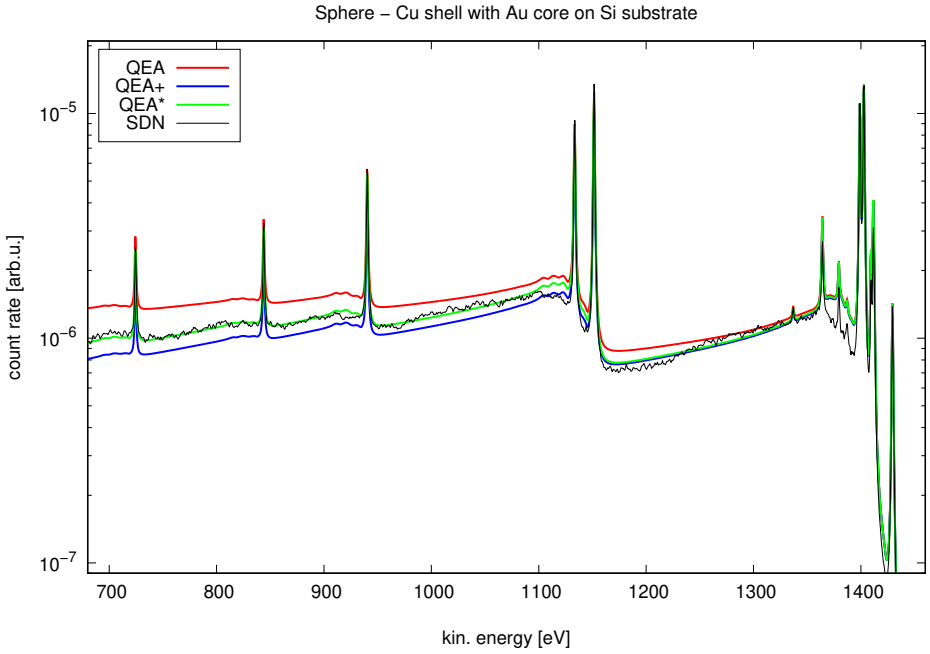

Figure 4.20: Comparison of different simulation methods for a CSNP with a Cu shell and an Au core on a Si substrate.

5 Summary and Conclusion

Nanoparticles with a PTFE core and a PMMA shell prepared by a project partner (PMO) were investigated in the course of an inter-laboratory (BAM, NPL, TUW) study with the goal to determine the feasibility of accurate shell thickness measurements with XPS. Although the non-trivial specimen preparation and the experimentally challenging sample measurements were done in different laboratories with distinct setups, the retrieved thicknesses were consistent within an experimental error below 10%.

Different thickness estimation methods (SESSA, IC-model, Shards T_{NP} formula) were applied to the measured XPS data and consistent thicknesses were determined by each method. Shards T_{NP} formula is a simple and a very accurate method to estimate the shell thicknesses of CSNP within specific conditions. Moreover the adaptability and simple usage of the SESSA program helps users to generate XPS spectra according to their experimental XPS setups to easily compare experimental and simulated XPS spectra. However, systematic inconsistencies in the thickness estimations were observed when the $F1s$ signal was used for the core. The most probable explanation is that fluorine diffuses from the core into the shell. Nevertheless, XPS and the applied thickness estimation methods have proven to be a consistent and good instrument for this task, allowing one to establish shell thicknesses with an accuracy of $\sim$10%.

Furthermore different transmission electron microscopy techniques (EDX, EELS, STEM) were applied to get a better understanding of the core-shell nanoparticles (CSNP) morphology and to verify the estimated thicknesses. Despite the verification of the estimated dimensions these investigations revealed that the majority of the CSNP exhibited asymmetries in the morphology. With the combination of electron beam analysis and X-ray photoelectron spectroscopy (XPS) a good understanding of the investigated PTFE@PMMA core-shell nanoparticles could be achieved.

Simulations of core-shell nanoparticles with asymmetric features were created - to model the actual observed CSNP morphologies as observed with the different analysis techniques. These simulations demonstrated the impact such features have on the peak intensity calculations, which is an important factor in the utilized methods for the shell thickness determination.

In summary it can be said that, by means of XPS spectra analysis the average shell thickness of an core-shell nanoparticle in an ensemble like a powder can be determined within an accuracy of about 10%.

Moreover, a new Monte Carlo model was implemented into SESSA and tested. For

different geometries and elements the default quasi-elastic approximation (QEA) model and the newly implemented true slowing down (SDN) model differ only for high energy losses which is expected as the QEA neglects the energy dependence of inelastic scattering events. Additional enhancements (QEA+, QEA*) for the default quasi-elastic approximation were tested and compared with the newly implemented SDN method showing promising results. These conceptually simple post processing techniques which are based on the energy dependence of the inelastic mean free path reproduce the XPS background simulated with the computationally intensive SDN method to a high degree.

6 Acknowledgements

First of all , I would like to thank my supervisor Wolfgang Werner for his support, guidance and impulses given while working on the project and completing my education at the Vienna University of Technology. His insight in physics, knowledge in the field and positive attitude left a mark and are an example for me in the future.

I am very grateful for clarifying discussions and suggestions by my institute colleagues Vytautas Astasauskas and Olga Ridzel. Their kindness, openness and support motivated me to complete my studies and made the work seem to be just another thing to do while enjoying their company.

For the help with the TEM measurements I am very grateful to Michael Stöger-Pollach. For assistance in obtaining the XPS measurements I would like to thank Markus Sauer. Without their expertise, experience and knowledge with these experimental methods obtaining the experimental data would have been impossible.

In addition I greatly acknowledge and thank my colleague Henryk Kalbe, for his work and guidance in the project. His enthusiasm was a very positive feedback which helped me fulfil the necessary work.

I am grateful to my predecessors Maksymilian Chudzicki and Johannes Pseiner and their work done at the institute and in this field, which helped me get insight into the field.

I am thankful for the open and clarifying discussions with Alex Shard (NPL, UK), David Cant (NPL, UK) and the other project colleagues. To get an deeper understanding of the investigated particles and in general a better overview of the field.

Finally, I am very grateful for my families' and friends' support and the motivation given along the way. Without their positive motivation, given impulses and supporting surrounding finishing my studies would not have been possible.

Research leading to results reported in this work were funded by the Innanopart 14IND12 project as part of the European Metrology Programme for Innovation and Research (EMPIR) initiative of the European Unions Horizon 2020 research and innovation program.

References

[1] nanohybrids.net. *Nanoparticles Approved in the United States (US) and Europe (EU) for Medical Applications*. 28th July 2017. URL: https://nanohybrids.net/pages/cleared-nanoparticles-for-medical-use (visited on 12/03/2019).

[2] ISO. *ISO/TS 80004-1:2015. Nanotechnologies – Vocabulary – Part 1: Core terms*. Version 2. International Organization for Standardization. Dec. 2015. URL: https://www.iso.org/standard/68058.html (visited on 14/02/2019).

[3] EU. *Definition of a nanomaterial*. 14th Feb. 2019. URL: http://ec.europa.eu/environment/chemicals/nanotech/faq/definition_en.htm.

[4] EU. *Commission Recommendation of 18 October 2011 on the definition of nanomaterial Text with EEA relevance*. Commission of the European Union. Oct. 2011. URL: https://eur-lex.europa.eu/legal-content/EN/TXT/?uri=CELEX:32011H0696 (visited on 14/02/2019).

[5] Goeran LOEVESTAM et al. *Considerations on a Definition of Nanomaterial for Regulatory Purposes*. Research rep. Institute for Health and Consumer Protection Historical Collection, 14th Feb. 2019. DOI: 10.2788/98686. eprint: https://ec.europa.eu/jrc/sites/jrcsh/files/jrc_reference_report_201007_nanomaterials.pdf. URL: https://publications.europa.eu/en/publication-detail/-/publication/3d67886b-9899-43d1-818f-b8bfb1868538/language-en (visited on 14/02/2019).

[6] Mélanie Auffan et al. "Towards a definition of inorganic nanoparticles from an environmental, health and safety perspective". In: *Nature Nanotechnology* 4.10 (Sept. 2009), pp. 634–641. DOI: 10.1038/nnano.2009.242.

[7] Bharat Bhushan. *Springer Handbook of Nanotechnology*. Ed. by Bharat Bhushan. Springer Berlin Heidelberg, 2nd Nov. 2017. ISBN: 3662543559. DOI: 10.1007/978-3-642-02525-9. URL: https://link.springer.com/book/10.1007%2F978-3-642-02525-9 (visited on 14/02/2019).

[8] Darrell R. Boverhof et al. "Comparative assessment of nanomaterial definitions and safety evaluation considerations". In: *Regulatory Toxicology and Pharmacology* 73.1 (Oct. 2015), pp. 137–150. DOI: 10.1016/j.yrtph.2015.06.001.

[9] Patrick Boisseau and Bertrand Loubaton. "Nanomedicine, nanotechnology in medicine". In: *Comptes Rendus Physique* 12.7 (Sept. 2011), pp. 620–636. DOI: 10.1016/j.crhy.2011.06.001.

[10] Ganesh Venkatraman et al. "Nanomedicine: towards development of patient-friendly drug-delivery systems for oncological applications". In: *International Journal of Nanomedicine* (Feb. 2012), p. 1043. DOI: 10.2147/ijn.s25182.

[11] Bradley Roth and Carolyn M. D'Almeida. "Medical Applications of Nanoparticles". In: *Meeting of Minds: Journal of Undergradaute Research* 15 (Jan. 2013), pp. 1–10. eprint: https://www.umflint.edu/sites/default/files/groups/Research_and_Sponsored_Programs/MOM/c.dalmeida_b.roth_.pdf. (Visited on 12/03/2019).

[12] EU. *Regulation (EC) No 1223/2009 of the European Parliament and of the Council of 30 November 2009 on cosmetic products*. 22nd Dec. 2009. URL: https://eur-lex.europa.eu/legal-content/EN/ALL/?uri=CELEX:32009R1223 (visited on 14/02/2019).

[13] EU. *Regulation (EU) No 1169/2011 of the European Parliament and of the Council of 25 October 2011 on the provision of food information to consumers*. 22nd Nov. 2011. URL:

https://eur-lex.europa.eu/legal-content/EN/TXT/?uri=celex:32011R1169 (visited on 14/02/2019).

[14] EU. *Regulation (EU) 2015/2283 of the European Parliament and of the Council of 25 November 2015 on novel foods*. 11th Dec. 2015. URL: https://eur-lex.europa.eu/legal-content/EN/TXT/?uri=CELEX:32015R2283 (visited on 12/03/2019).

[15] INNANOPART. *Project objectives*. URL: http://empir.npl.co.uk/innanopart/objectives/ (visited on 25/09/2018).

[16] Alexander G. Shard. "A Straightforward Method For Interpreting XPS Data From Core–Shell Nanoparticles". In: *The Journal of Physical Chemistry C* 116.31 (July 2012), pp. 16806–16813. DOI: 10.1021/jp305267d. eprint: https://pubs.acs.org/doi/pdf/10.1021/jp305267d. (Visited on 12/03/2019).

[17] H. Kalbe, S. Rades and W. E. S. Unger. "Determining shell thicknesses in stabilised CdSe@ZnS core-shell nanoparticles by quantitative XPS analysis using an Infinitesimal Columns model". In: *Journal of Electron Spectroscopy and Related Phenomena* 212 (1st Oct. 2016), pp. 34–43. DOI: 10.1016/j.elspec.2016.08.002.

[18] S. Tougaard. "Surface nanostructure determination by x-ray photoemission spectroscopy peak shape analysis". In: *Journal of Vacuum Science & Technology A: Vacuum, Surfaces, and Films* 14.3 (May 1996), pp. 1415–1423. DOI: 10.1116/1.579963. eprint: http://www.quases.com/data/documents/103=20Surf=20Nanostructure=20determination=20by=20XPS=20peak=20shape=20analysis.pdf.

[19] Terry L. Alford, L. C. Feldman and James W. Mayer. *Fundamentals of Nanoscale Film Analysis*. Springer US, 16th Feb. 2007. 352 pp. ISBN: 0387292608. URL: https://link.springer.com/book/10.1007%2F978-0-387-29261-8 (visited on 04/10/2018).

[20] D. Briggs and John T. Grant. *Surface Analysis by Auger and X-Ray Photoelectron Spectroscopy*. IM Publications, 2003. ISBN: 1901019047. URL: https://www.surfaceanalysis.org/BriggsGrant.html (visited on 04/10/2018).

[21] John F. Watts and John Wolstenholme. *An Introduction to Surface Analysis by XPS and AES*. Wiley, 2003. ISBN: 9780470847138.

[22] NobelPrize.org. *Kai M. Siegbahn*. Ed. by Nobel Media AB. 2019. URL: https://www.nobelprize.org/prizes/physics/1981/siegbahn/ (visited on 19/02/2019).

[23] Robley Dunglison Evans. *The atomic nucleus*. International series in pure and applied physics. McGraw-Hill, 1955. eprint: https://archive.org/details/atomicnucleus032805mbp. URL: https://books.google.at/books?id=6sLQAAAAMAAJ (visited on 04/10/2018).

[24] C. M. Davisson. "Interaction of γ-radiation with matter". In: *Alpha-, Beta- and Gamma-Ray Spectroscopy*. Elsevier, 1968, pp. 37–78. DOI: 10.1016/b978-0-7204-0083-0.50007-9.

[25] K. Siegbahn and C. Nordling. *Atomic, Molecular and Solid State Structure Studied by Means of Electron Spectroscopy*. Acta Universitatis Upsaliensis: Nova acta Regiae Societatis Scientiarum Upsaliensis. Kungl. Vetenskaps-societeten i Uppsala, 1967, p. 283.

[26] Ulflund. *X-Ray range*. URL: https://commons.wikimedia.org/wiki/File:X-ray_range.svg (visited on 09/10/2018).

[27] Philip L. Salmon and Xuan Liu. "MicroCT Bone Densitometry: Context Sensitivity, Beam Hardening Correction and the Effect of Surrounding Media". In: *The Open Access Journal of Science and Technology* 2 (2014), pp. 1–25. DOI: 10.11131/2014/101142. URL: http://www.agialpress.com/journals/oajost/2014/101142/ (visited on 04/10/2018).

[28] A. Einstein. "Über einen die Erzeugung und Verwandlung des Lichtes betreffenden heuristischen Gesichtspunkt". In: *Annalen der Physik* 322.6 (1905), pp. 132–148. DOI: 10.1002/andp.19053220607.

[29] G. Beamson and D. Briggs. *High Resolution XPS of Organic Polymers: The Scienta ESCA300 Database*. Wiley, 1992. ISBN: 0471935921.

[30] R. F. Schwitters. *Scattering and Decays from Fermi's Golden Rule including all the h's and c's*. 8th Oct. 2018. URL: https://web2.ph.utexas.edu/~schwitte/PHY362L/QMnote.pdf.

[31] P. A. M. Dirac. "The Quantum Theory of the Emission and Absorption of Radiation". In: *Proceedings of the Royal Society A: Mathematical, Physical and Engineering Sciences* 114.767 (Mar. 1927), pp. 243–265. DOI: 10.1098/rspa.1927.0039.

[32] Enrico Fermi. *Nuclear Physics. A Course Given by Enrico Fermi at the University of Chicago*. University of Chicago Press, 11th Aug. 1974. 258 pp. ISBN: 0226243656. URL: http://fermi.lib.uchicago.edu/fermicollection.htm.

[33] M. B. Trzhaskovskaya, V. I. Nefedov and V. G. Yarzhemsky. "Photoelectron angular distribution parameters for elements Z=1 to Z=54 in the photoelectron energy range 100–5000 eV". In: *Atomic Data and Nuclear Data Tables* 77.1 (Jan. 2001), pp. 97–159. DOI: 10.1006/adnd.2000.0849.

[34] M. B. Trzhaskovskaya, V. I. Nefedov and V. G. Yarzhemsky. "Photoelectron angular distribution parameters for elements Z=55 to Z=100 in the photoelectron energy range 100–5000 eV". In: *Atomic Data and Nuclear Data Tables* 82.2 (Nov. 2002), pp. 257–311. DOI: 10.1006/adnd.2002.0886.

[35] Lise Meitner. "Über die β-Strahl-Spektra und ihren Zusammenhang mit der γ-Strahlung". In: *Zeitschrift für Physik* 11.1 (Dec. 1922), pp. 35–54. DOI: 10.1007/bf01328399.

[36] Wolfgang S. M. Werner. "Electron transport in solids for quantitative surface analysis". In: *Surface and Interface Analysis* 31.3 (2001), pp. 141–176. DOI: 10.1002/sia.973. eprint: https://onlinelibrary.wiley.com/doi/epdf/10.1002/sia.973.

[37] Jörg Zegenhagen and Christof Kunz. "Proceedings of the Workshop on Hard X-ray Photoelectron Spectroscopy". In: *Nuclear Instruments and Methods in Physics Research Section A: Accelerators, Spectrometers, Detectors and Associated Equipment* 547.1 (July 2005), p. v. DOI: 10.1016/j.nima.2005.05.002.

[38] H. Hafner, J. Arol Simpson and C. E. Kuyatt. "Comparison of the Spherical Deflector and the Cylindrical Mirror Analyzers". In: *Review of Scientific Instruments* 39.1 (Jan. 1968), pp. 33–35. DOI: 10.1063/1.1683103.

[39] W. S. M. Werner, W. Smekal and C. J. Powell. *Simulation of electron spectra for surface analysis (SESSA) version 2.1 user's guide*. Tech. rep. Dec. 2017. DOI: 10.6028/nist.nsrds.100-2017. (Visited on 27/10/2018).

[40] Werner Smekal, Wolfgang S. M. Werner and Cedric J. Powell. "Simulation of electron spectra for surface analysis (SESSA): a novel software tool for quantitative Auger-electron spectroscopy and X-ray photoelectron spectroscopy". In: *Surface and Interface Analysis* 37.11 (2005), pp. 1059–1067. DOI: 10.1002/sia.2097.

[41] J. Baró et al. "PENELOPE: An algorithm for Monte Carlo simulation of the penetration and energy loss of electrons and positrons in matter". In: *Nuclear Instruments and Methods in Physics Research Section B: Beam Interactions with Materials and Atoms* 100.1 (May 1995), pp. 31–46. DOI: 10.1016/0168-583x(95)00349-5.

[42] Francesc Salvat, José Fernández-Varea and Josep Sempau. "PENELOPE2008: A Code System for Monte Carlo Simulation of Electron and Photon Transport". In: *Workshop Proceedings, Data Bank NEA/NSC/DOC(2011)5, Barcelona* (July 2006). eprint: https://www.oecd-nea.org/science/pubs/2009/nea6416-penelope.pdf. (Visited on 27/10/2018).

[43] I. S. Tilinin, A. Jablonski and W. S. M. Werner. "Quantitative surface analysis by Auger and x-ray photoelectron spectroscopy". In: *Progress in Surface Science* 52.4 (Aug. 1996), pp. 193–335. DOI: 10.1016/0079-6816(96)00008-1.

[44] Wolfgang S. M. Werner. "Partial intensity analysis (PIA) for quantitative electron spectroscopy". In: *Surface and Interface Analysis* 23.11 (Oct. 1995), pp. 737–752. DOI: 10.1002/sia.740231103.

[45] I. S. Tilinin and W. S. M. Werner. "Angular and energy distribution of Auger and photoelectrons escaping from non-crystalline solid surfaces". In: *Surface Science* 290.1-2 (June 1993), pp. 119–133. ISSN: 0039-6028. DOI: 10.1016/0039-6028(93)90594-a. URL: http://www.sciencedirect.com/science/article/pii/003960289390594A.

[46] Wolfgang S. M. Werner. "Slowing down of medium-energy electrons in solids". In: *Physical Review B* 55.22 (June 1997), pp. 14925–14934. DOI: 10.1103/physrevb.55.14925.

[47] Peter Schattschneider. *Fundamentals of Inelastic Electron Scattering*. Springer Vienna, 1986. DOI: 10.1007/978-3-7091-8866-8.

[48] W. H. Gries and W. Werner. "Take-off angle and film thickness dependences of the attenuation length of X-ray photoelectrons by a trajectory reversal method". In: *Surface and Interface Analysis* 16.1-12 (July 1990), pp. 149–153. DOI: 10.1002/sia.740160129.

[49] M. P. Seah and W. A. Dench. "Quantitative electron spectroscopy of surfaces: A standard data base for electron inelastic mean free paths in solids". In: *Surface and Interface Analysis* 1.1 (Feb. 1979), pp. 2–11. DOI: 10.1002/sia.740010103.

[50] C. D. Wagner, L. E. Davis and W. M. Riggs. "The energy dependence of the electron mean free path". In: *Surface and Interface Analysis* 2.2 (Apr. 1980), pp. 53–55. DOI: 10.1002/sia.740020204.

[51] S. Tanuma, C. J. Powell and D. R. Penn. "Calculations of electron inelastic mean free paths (IMFPS). IV. Evaluation of calculated IMFPs and of the predictive IMFP formula TPP-2 for electron energies between 50 and 2000 eV". In: *Surface and Interface Analysis* 20.1 (Jan. 1993), pp. 77–89. DOI: 10.1002/sia.740200112.

[52] C. J. Powell and A. Jablonski. "Progress in quantitative surface analysis by X-ray photoelectron spectroscopy: Current status and perspectives". In: *Journal of Electron Spectroscopy and Related Phenomena* 178-179 (May 2010), pp. 331–346. DOI: 10.1016/j.elspec.2009.05.004.

[53] M. Chudzicki et al. "Evaluating the Internal Structure of Core–Shell Nanoparticles Using X-ray Photoelectron Intensities and Simulated Spectra". In: *The Journal of Physical Chemistry C* 119.31 (July 2015), pp. 17687–17696. DOI: 10.1021/acs.jpcc.5b04517.

[54] Peter J. Cumpson. "The Thickogram: a method for easy film thickness measurement in XPS". In: *Surface and Interface Analysis* 29.6 (2000), pp. 403–406. DOI: 10.1002/1096-9918(200006)29:6<403::aid-sia884>3.0.co;2-8.

[55] A. G. Shard, J. Wang and S. J. Spencer. "XPS topofactors: determining overlayer thickness on particles and fibres". In: *Surface and Interface Analysis* 41.7 (July 2009), pp. 541–548. DOI: 10.1002/sia.3044.

[56] S. Tanuma, C. J. Powell and D. R. Penn. "Calculations of electron inelastic mean free paths. V. Data for 14 organic compounds over the 50-2000 eV range". In: *Surface and Interface Analysis* 21.3 (Mar. 1994), pp. 165–176. DOI: 10.1002/sia.740210302.

[57] Johannes Pseiner. "Quantification of X-ray photoelectron data from core-shell nanoparticles. Quantifizierung von XPS-daten von Kern-Schalen-Nanopartikeln". MA thesis. Technische Universität Wien | Fakultät für Physik | Institut für Angewandte Physik | E134, 21st Sept. 2016. 78 pp. eprint: http://repositum.tuwien.ac.at/obvutwhs/download/pdf/1517040. URL: http://repositum.tuwien.ac.at/urn:nbn:at:at-ubtuw:1-7392 (visited on 15/01/2019).

[58] Wolfgang S. M. Werner et al. "Interpretation of nanoparticle X-ray photoelectron intensities". In: *Applied Physics Letters* 104.24 (June 2014), p. 243106. DOI: 10.1063/1.4884065.

Appendices

SAMPLES WP3

PTFE (Hyflon®) Seed Particles

kindly supplied by Solvay Specialty Polymers (refractive index 1.331)

Sample	D_{SEM} nm	STD_{SEM} nm
Hyflon	47	8

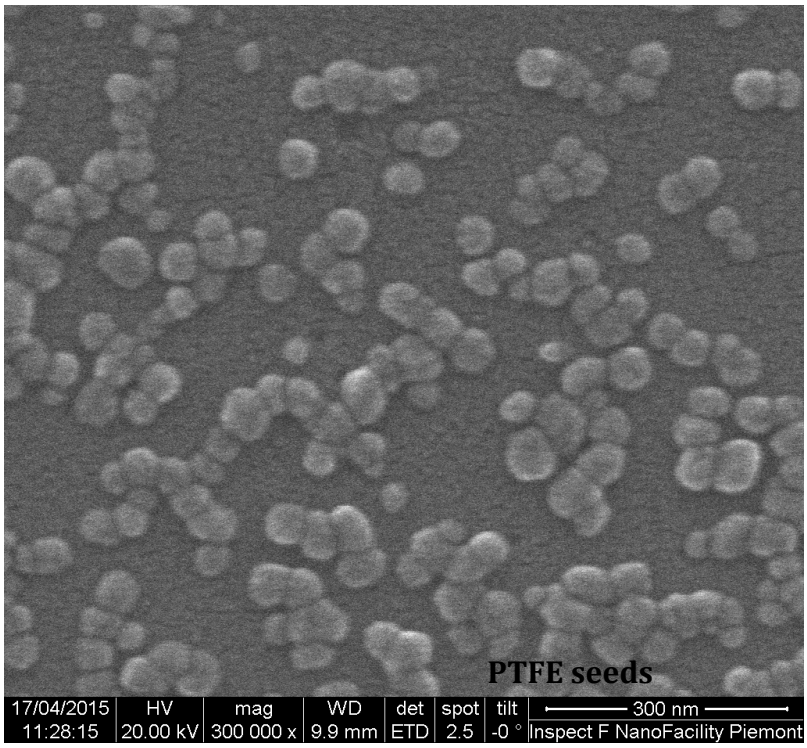

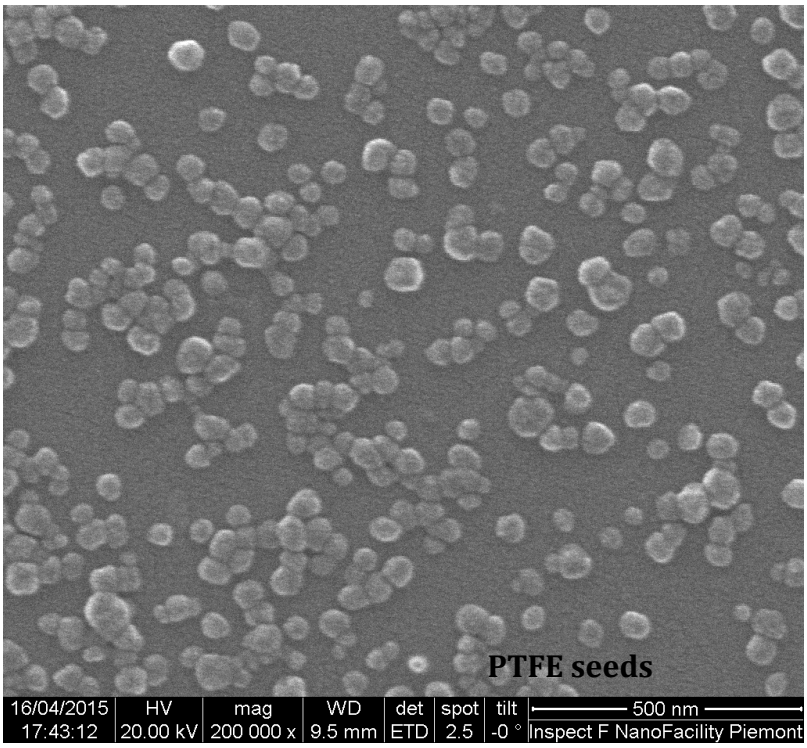

PTFE/PS Core-shell nanoparticles

(PS refractive index 1.5915 at 589 nm)

Sample	D_{SEM} nm	STD_{SEM} nm	Shell nm	D_{PCS} nm	PDI_{PCS}	Solid Content mg/ml
HS1	59	6	6	63	0.056	68.2
HS3	68	5	10	71	0.036	110.0
HS5	81	5	17	84	0.019	129.2
HS6	94	5	24	98	0.024	127.8
HS7	115	4	34	120	0.030	103.2
HS8	143	4	48	159	0.008	88.6

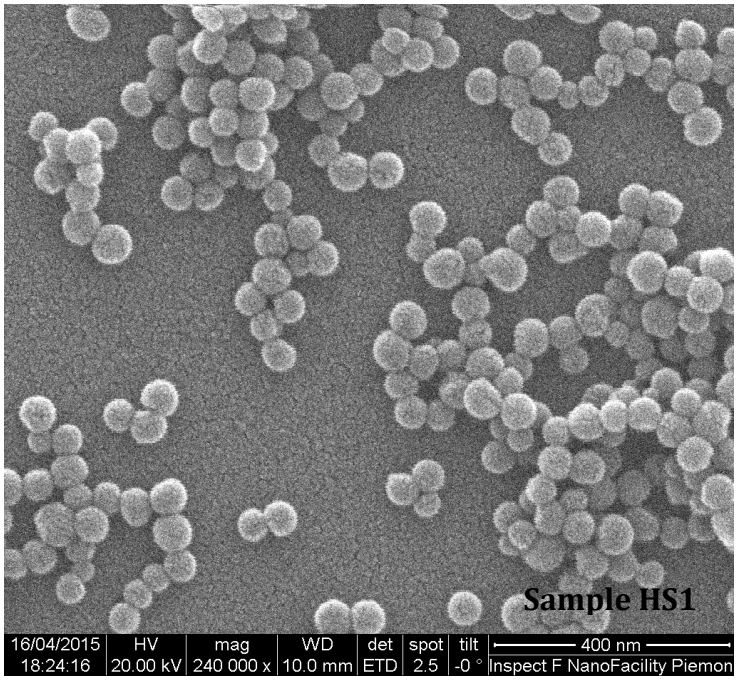

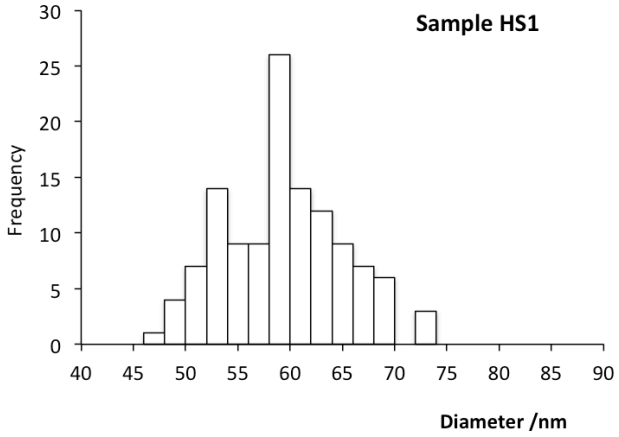

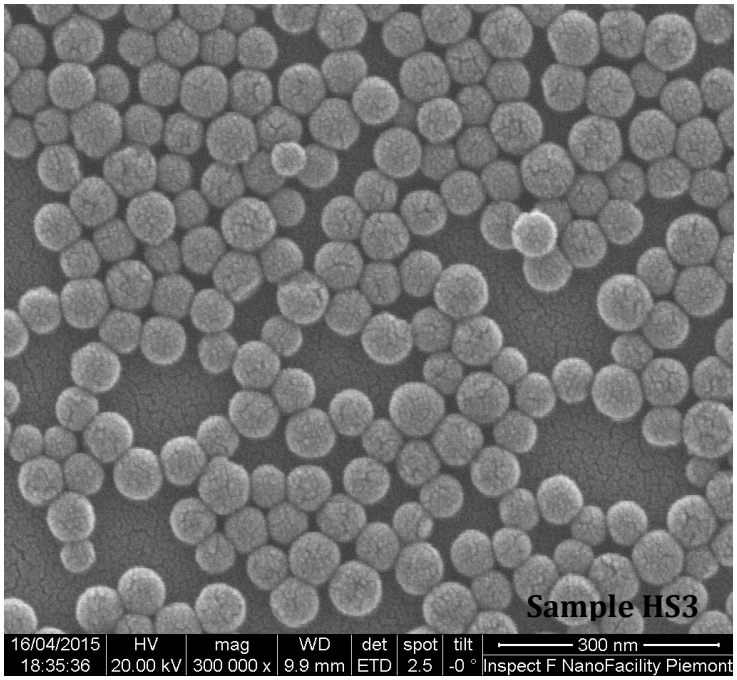

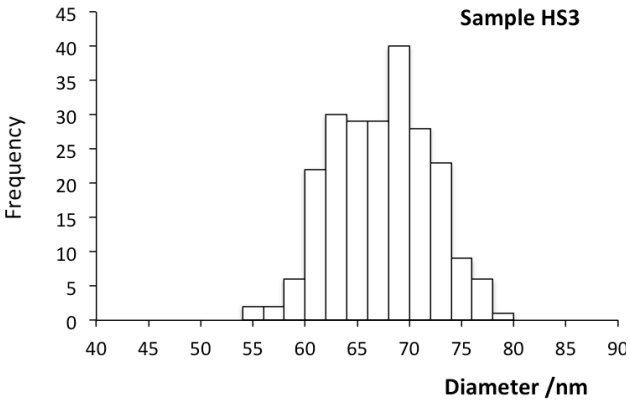

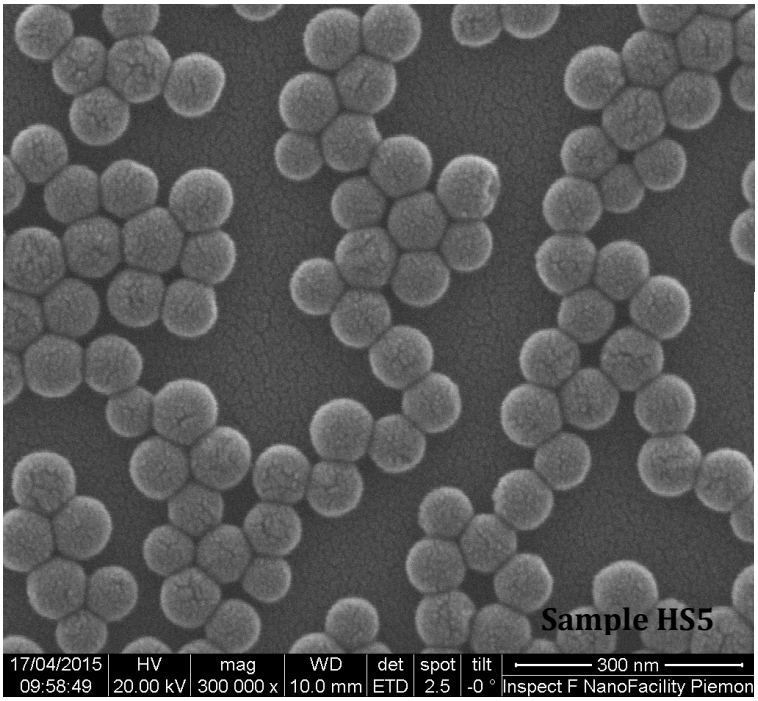
Sample HS5
17/04/2015 09:58:49
HV 20.00 kV
mag 300 000 x
WD 10.0 mm
det ETD
spot 2.5
tilt -0 °
300 nm
Inspect F NanoFacility Piemon

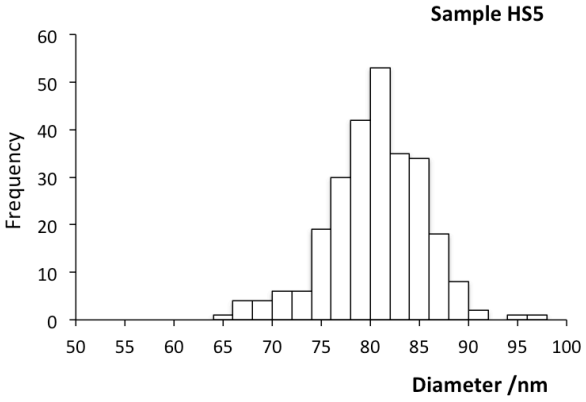
Sample HS5
Frequency
0
10
20
30
40
50
60
50 55 60 65 70 75 80 85 90 95 100
Diameter /nm

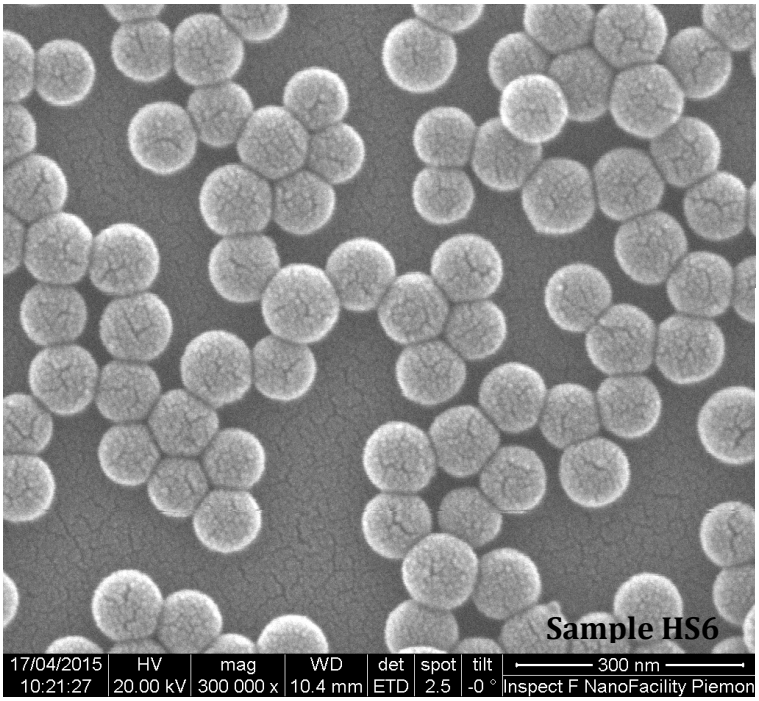
Sample HS6
17/04/2015 10:21:27
HV 20.00 kV
mag 300 000 x
WD 10.4 mm
det ETD
spot 2.5
tilt -0 °
300 nm
Inspect F NanoFacility Piemon

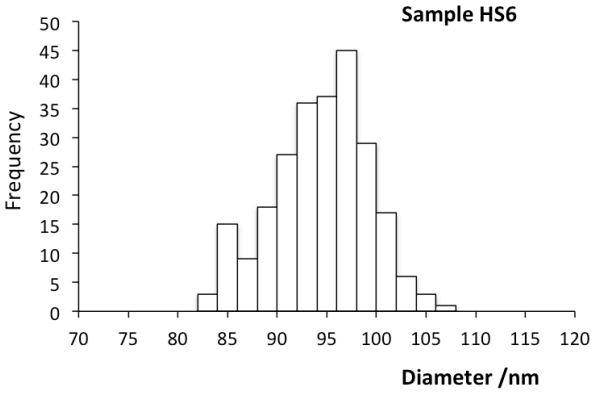
Sample HS6
Frequency
0
5
10
15
20
25
30
35
40
45
50
70 75 80 85 90 95 100 105 110 115 120
Diameter /nm

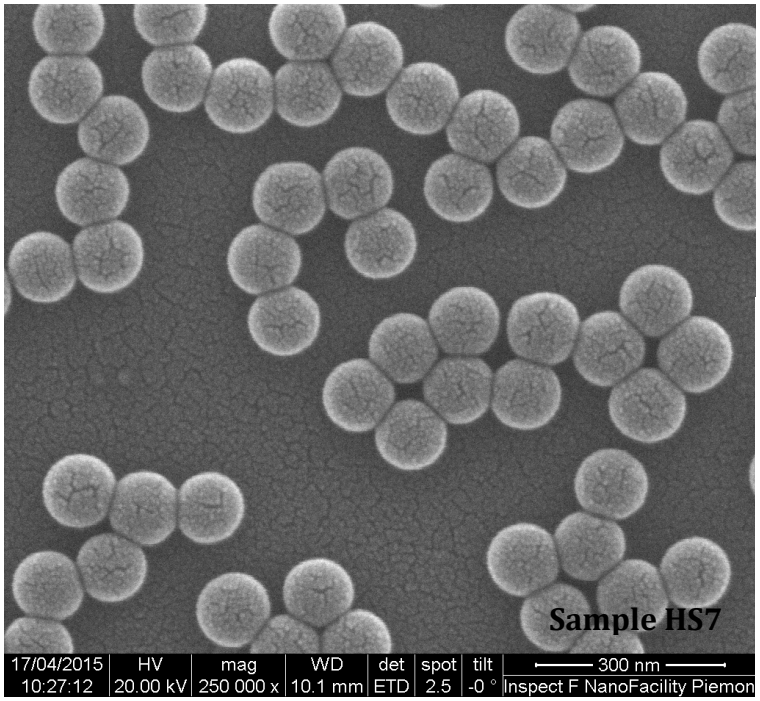
Sample HS7
17/04/2015 10:27:12
HV 20.00 kV
mag 250 000 x
WD 10.1 mm
det ETD
spot 2.5
tilt -0 °
300 nm
Inspect F NanoFacility Piemon

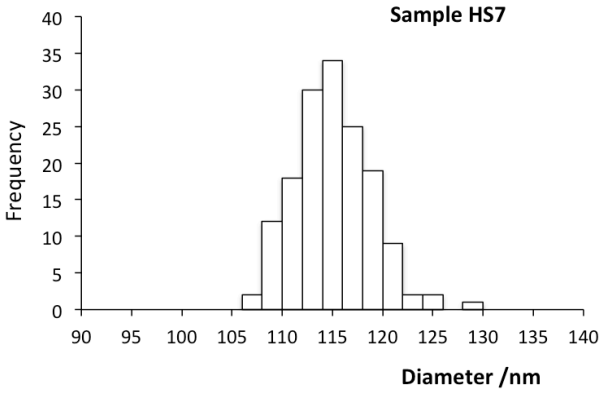
Sample HS7
Frequency
Diameter /nm
0
5
10
15
20
25
30
35
40
90
95
100
105
110
115
120
125
130
135
140

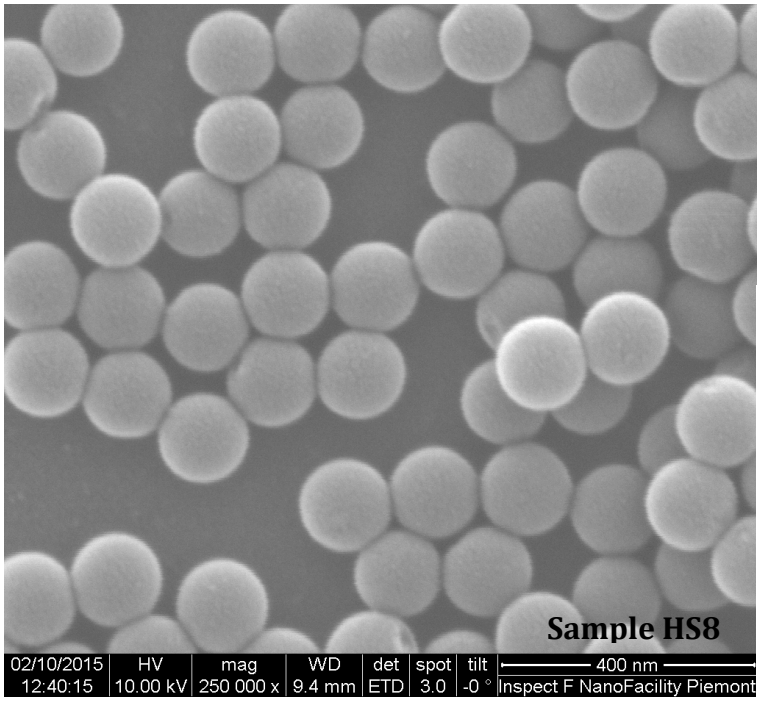
Sample HS8
02/10/2015 12:40:15
HV 10.00 kV
mag 250 000 x
WD 9.4 mm
det ETD
spot 3.0
tilt -0 °
400 nm
Inspect F NanoFacility Piemont

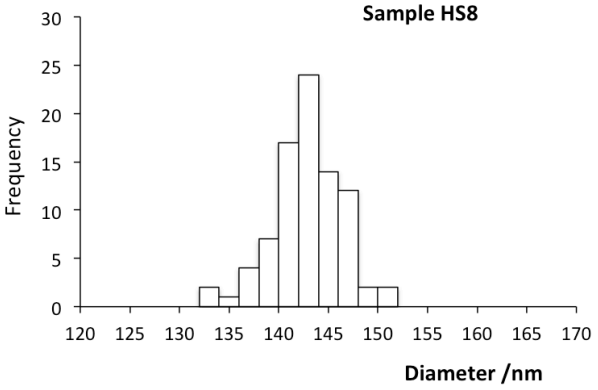
Sample HS8
Frequency
Diameter /nm
0
5
10
15
20
25
30
120
125
130
135
140
145
150
155
160
165
170

PTFE/PMMA Core-shell nanoparticles

(PMMA refractive index 1.4906 at 589 nm)

Sample	D_{SEM} nm	STD_{SEM} nm	Shell nm	D_{PCS} nm	PDI_{PCS}	Solid Content mg/ml
HM3	56	6	4.5	73	0.043	90.5
HM5	71	5	12	94	0.046	109.2
HM7	94	4	23.5	123	0.042	81.8
HM8	118	3	35.5	160	0.029	60.4

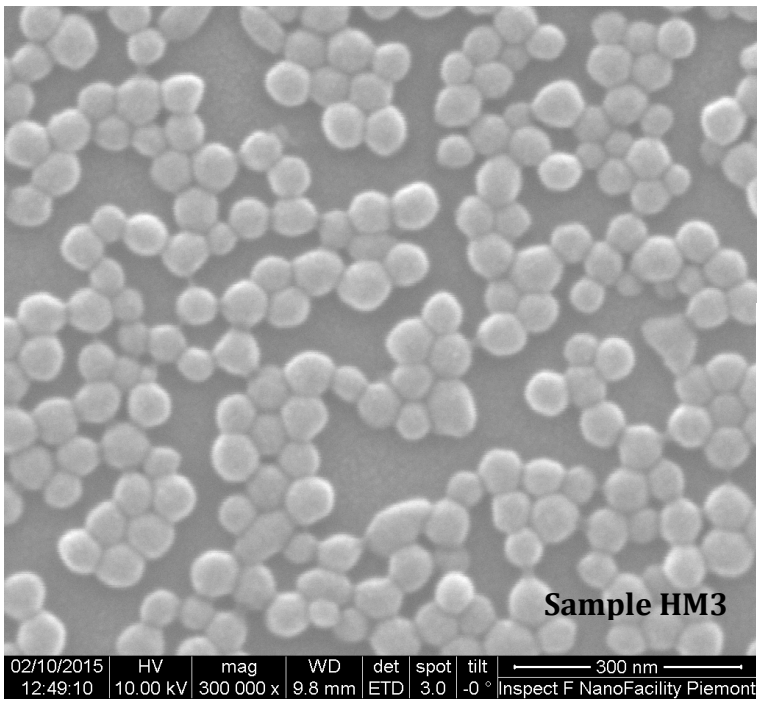

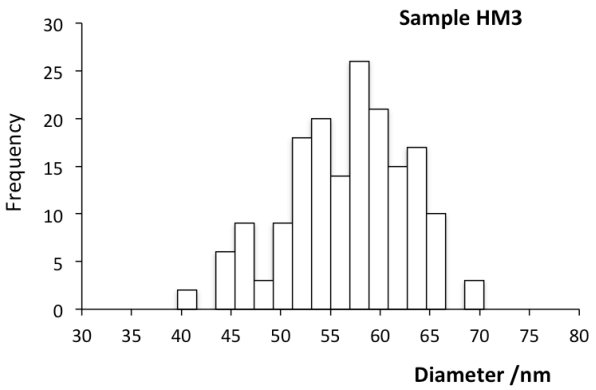

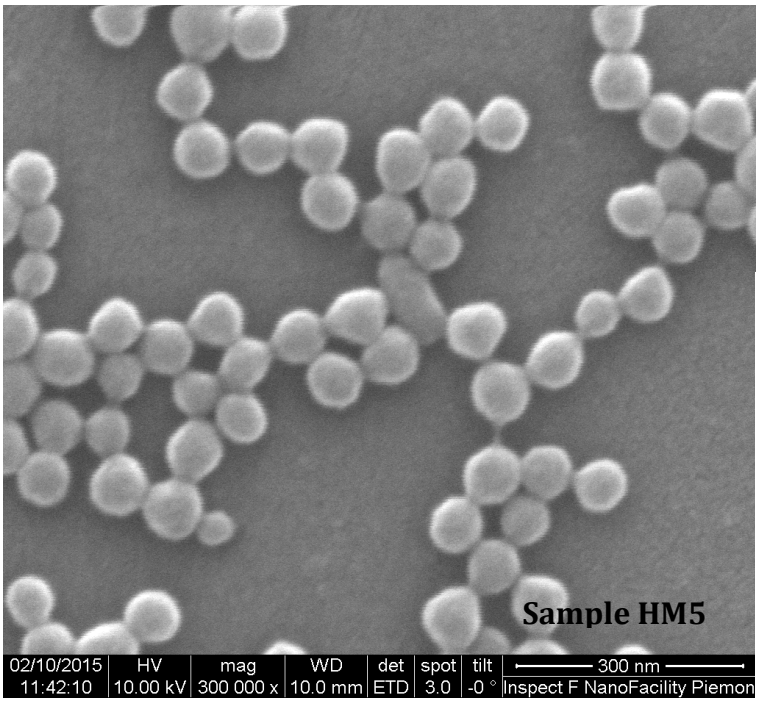

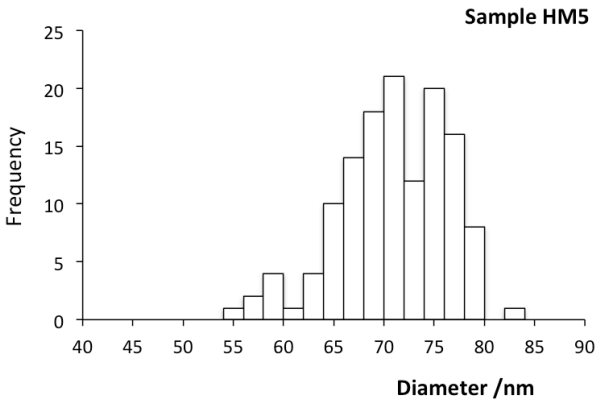

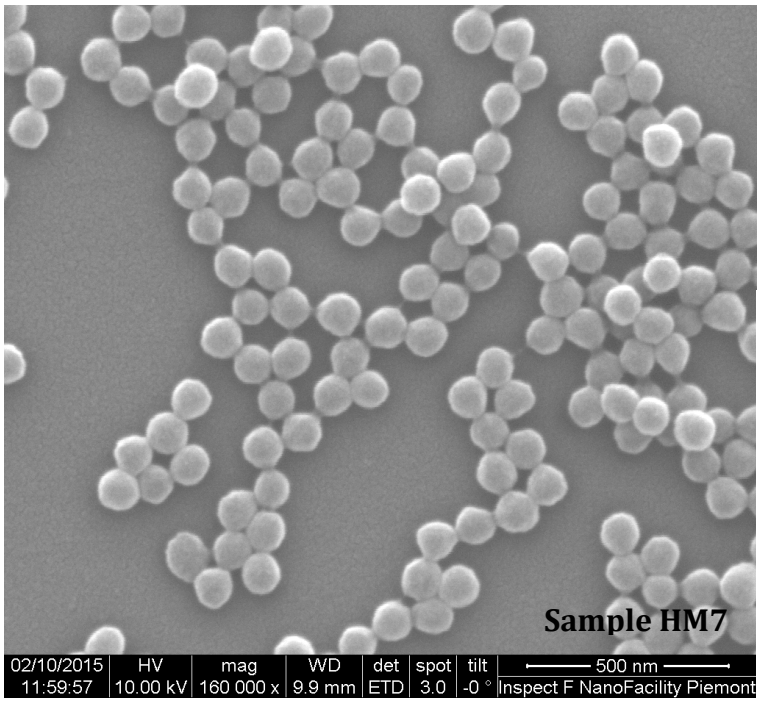
Sample HM7
02/10/2015 | HV | mag | WD | det | spot | tilt | 500 nm
11:59:57 | 10.00 kV | 160 000 x | 9.9 mm | ETD | 3.0 | -0 ° | Inspect F NanoFacility Piemont

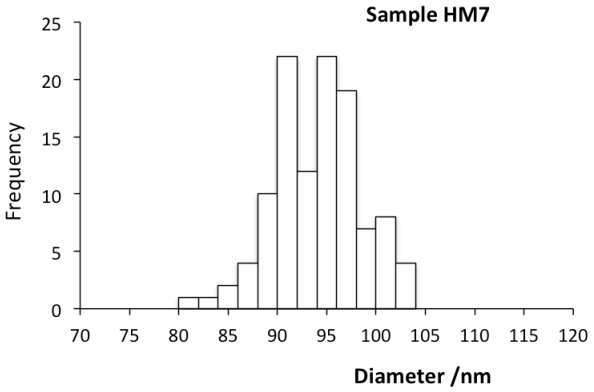
Sample HM7
Frequency
0
5
10
15
20
25
70
75
80
85
90
95
100
105
110
115
120
Diameter /nm

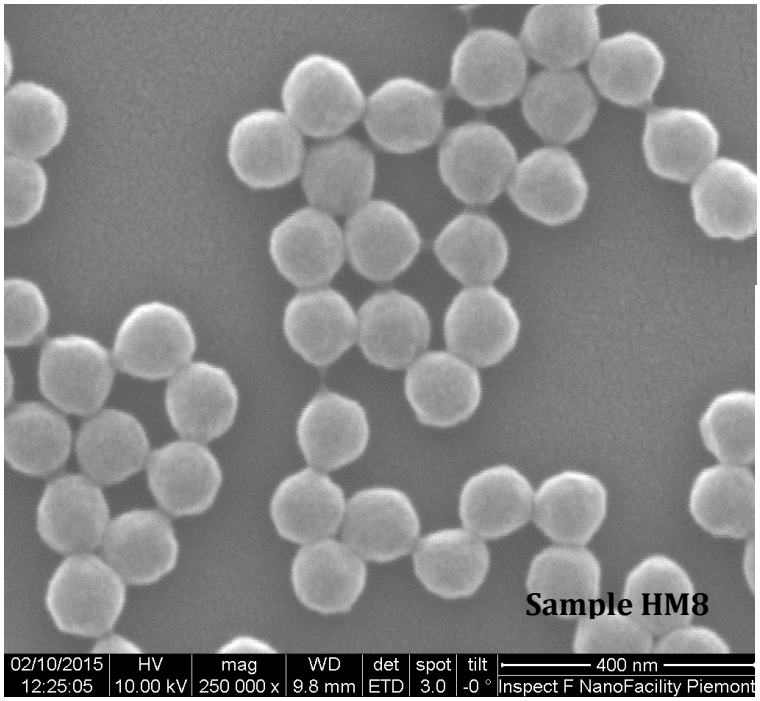
Sample HM8
02/10/2015 | HV | mag | WD | det | spot | tilt | 400 nm
12:25:05 | 10.00 kV | 250 000 x | 9.8 mm | ETD | 3.0 | -0 ° | Inspect F NanoFacility Piemont

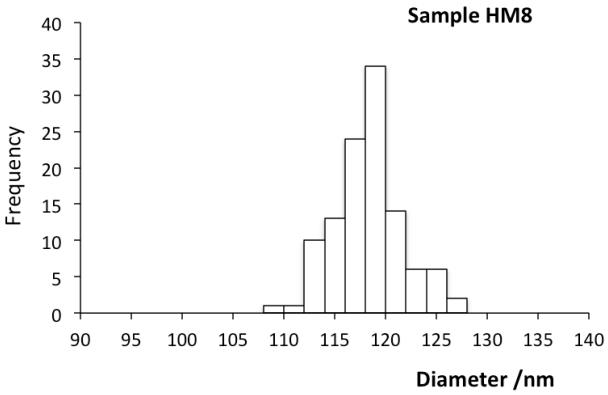
Sample HM8
Frequency
0
5
10
15
20
25
30
35
40
90
95
100
105
110
115
120
125
130
135
140
Diameter /nm